IEEE Access
Multidisciplinary | Rapid Review | Open Access Journal

Received 17 November 2023, accepted 21 November 2023, date of publication 30 November 2023,
date of current version 6 December 2023.

*Digital Object Identifier 10.1109/ACCESS.2023.3337823*

RESEARCH ARTICLE

# Dual-Layer Metamaterial Rectangular Antenna Arrays for In-Band Full-Duplex Massive MIMO

**YUANZHE GONG, (Graduate Student Member, IEEE), MOBEEN MAHMOOD, (Graduate Student Member, IEEE), ROBERT MORAWSKI, AND THO LE-NGOC, (Life Fellow, IEEE)**
Department of Electrical and Computer Engineering, McGill University, Montreal, QC H3A 0E9, Canada

Corresponding author: Yuanzhe Gong (yuanzhe.gong@mail.mcgill.ca)

This work was supported in part by the Natural Sciences and Engineering Research Council of Canada, and in part by Huawei Technologies Canada.

**ABSTRACT** This paper presents a prototype pair of dual-layer electromagnetic bandgap slotted circularly polarized patch 8 × 8Tx/8 × 8Rx orthogonally-polarized antenna arrays designed for in-band full-duplex massive MIMO. The design processes of the antenna array, beamforming feeding network, and beam steering algorithms are discussed. The proposed prototype operates in a bandwidth of 250 MHz (or 7.1% at 3.5 GHz) from 3.35 GHz to 3.6 GHz. Using orthogonal Tx/Rx polarization, an average mutual coupling between any two Tx and Rx antenna elements of −49.2 dB can be achieved. Further improvement in Tx-to-Rx isolation at the beam level can be achieved with the two proposed beamforming schemes. Illustrative results using Tx/Rx 1 × 4 sub-arrays indicate the formed beams with an average mutual coupling of −65.6 dB between any two Tx and Rx beams (i.e., an improvement of 16.4 dB in Tx/Rx isolation). The sample Tx and Rx far-field beam patterns, radiation null depth and position, and corresponding Tx-to-Rx mutual coupling levels are investigated, which gives insight into the beamforming isolation improvement design. Within a steering range from −50 to 50 degrees, a directivity over 10.7 dB, a 3dB-beamwidth narrower than 33.0 degrees, and a normalized sidelobe level lower than −9.0 dB are achieved. Simulation and measurement results on the mutual coupling, beamforming directivity, beamwidth, and radiation patterns in various scenarios are investigated and found to be in good agreement.

**INDEX TERMS** Antenna isolation, array beam, beamforming, full-duplex, massive MIMO, mutual coupling, sub-array radiation patterns, self-interference cancellation.

## I. INTRODUCTION

Wireless service providers navigate a rapidly evolving technological landscape, driven by escalating demands for faster data speeds, greater spectrum efficiency, expanded capacity, and more robust channels. Massive multiple-input and multiple-output (massive MIMO) is considered one of the most promising technologies for future wireless systems. The total system capacity can be expanded almost linearly with respect to the minimum number of transmitters and receivers used in the system [1], [2]. Employing large-scale antenna arrays enables the system to generate directional beams with high directivity and narrow beamwidth, leading to an improvement in power efficiency and a reduction of spatial correlation. Beamforming focuses and directs the transmission or reception of the signal in specific directions, considerably boosting the signal strength and expanding the coverage range. By dynamically configuring sub-arrays to form multiple beams, the massive MIMO system can serve multiple users from various directions concurrently, greatly enhancing spectral efficiency and system throughput [3]. Furthermore, compared with half-duplex (HD) communications, full-duplex (FD) technologies can theoretically double the spectral efficiency with a reduced latency by simultaneously receiving and transmitting in the same frequency band [4]. The combination of FD and massive MIMO offers great potential to address the throughput and latency requirements of future wireless communication systems,

The associate editor coordinating the review of this manuscript and approving it for publication was Hassan Tariq Chattha.

especially in situations where spectrum resources are limited [5].

To fulfill the needs of the two technologies, the large-scale arrays play pivotal roles in addressing self-interference (SI) mitigation, a critical challenge in the design of FD massive MIMO systems. Since path loss quickly increases with the distance and the local Rx antenna is much closer to the Tx antenna than the remote users, the received signal power from the intended users can be significantly lower than the SI power. This strong SI can severely degrade the signal-to-interference-and-noise ratio (SINR), consequently limiting channel throughput [6]. To counter this issue, multiple-stage SI isolation and cancellation techniques can be employed in the large-scale array design, including RF power attenuation, beamforming isolation, and analog and digital canceller design [7], [8], [9]. The goal is to suppress the residual SI level at or below the noise floor, ensuring optimal FD performance.

To address the challenging issue of mitigating transmitter-to-receiver (Tx-to-Rx) mutual coupling (MC) and suppressing strong SI, the primary focus lies in the antenna isolation approach, which does not rely on channel information. This approach effectively safeguards against strong SI, preventing saturation of the analog-to-digital converter (ADC) and facilitating a smoother baseband precoding stage. It can be achieved via various passive isolation design techniques including Tx-to-Rx separation [10], [11], Tx-to-Rx cross-polarization [12], [13], employing frequency-selective surface (FSS) structures [14], [15], and by adding metamaterial absorber [16], [17]. Each of these techniques can offer 10 dB to 20 dB isolation improvement.

The residual SI can be further reduced via analog or digital canceller, where the main goal is to construct the SI estimate and then subtract it from the received signal at the analog front-end of the local Rx and thus, reduce the SI signal [18], [19], [20], [21]. It is shown that 25 dB to 50 dB SI cancellation can be achieved [22], [23], [24]. However, the cancellation performance is usually limited by hardware imperfections and comes with the drawbacks of relying heavily on accurate SI channel estimation and demanding high hardware complexity [21], [25]. Given the proliferation of components in large-scale array systems, the implementation of SI cancellation poses a substantial challenge in the FD massive MIMO systems.

Meanwhile, introducing large-scale arrays provides a new avenue to enhance isolation by controlling directional beams. Within a confined scattering propagation area, the beamforming can significantly diminish the intensity of leakage waves travelling toward interference directions, i.e., towards the local Rx. Experimental results in [26] show that using a directional rather than a monopole non-directional antenna can enhance isolation by about 17 dB in low-reflection environments. Furthermore, beamforming is important in controlling the interactions between beams and effectively attenuating SI. By electronically steering the beam towards the radiation null of the interference source, the intensity of direct path MC can be significantly reduced, allowing for efficient management of interference and enhancing overall system performance.

### A. RELATED WORKS

The shift to large-scale arrays represents a significant advancement in wireless technology, allowing next-generation networks to handle the immense and growing data traffic. The large physical size, however, creates challenges when it comes to manufacturing, installation, and adaptability as the number of elements increases. Thanks to its adjustable permittivity and permeability, metamaterials have emerged as a highly promising technology for overcoming the challenges in conventional array design [27], [28], [29]. Inserting resonate structures such as split ring resonators (SRR) in the dielectric substrate can enhance the effective permeability or permittivity, resulting in a reduced resonate frequency and a miniaturized antenna [30], [31]. However, these techniques often require the integration of metamaterial cells into the dielectric substrates, adding complexity to the manufacturing process and leading to bulky substrates. Studies in [14] and [32] introduced a miniaturized patch antenna design that leverages slow wave propagation within multi-layer metamaterial patch structures via creating constructive interference between the coupling waves. Without resorting to the insertion of periodic structures into the dielectric substrate, this method demonstrates great versatility across various array designs.

To ensure optimal FD communications, numerous techniques have been introduced in the realm of antenna isolation. The most direct method is increasing the separation distance between the Tx and the local Rx antennas to increase the path loss. Experiments show that a 65 dB to 85 dB attenuation can be reached with a separation distance of 3.5m to 5m [10], [11]. However, the compactness requirements of the overall system often impose limitations on the permissible separation distance between antennas in practical FD design. Furthermore, cross-polarization increases the polarization mismatch between the Tx and the local Rx antenna while decreasing the strength of leakage MC waves being captured by its local Rx antenna. It is demonstrated that orthogonal polarization can increase isolation by 10 to 18 dB [12], [13]. In [33], a proposed $2 \times 2$ cross-polarized FD prototype achieving a Tx-to-Rx isolation exceeding 45 dB under various test scenarios is demonstrated. Furthermore, by integrating Tx/Rx cross-polarization with both antenna port spacing and grounding via shorting pins techniques, an isolation level of 52 dB can be realized, as illustrated in [34]. Additionally, [35] and [36] present two 4-element FD antenna designs equipped with feeding phase control, designed for out-of-phase near-field coupling wave cancellation. Experimental measurement outcomes have reported a Tx-to-Rx isolation more than 40 dB. However, the addition of signal cancellation mechanisms within the feeding networks can potentially lead to excessive implementation complexity in the large-scale

antenna array design. Moreover, the integration of various structures, such as FSS, defected ground structures (DGS), and absorber structures, can effectively diminish, cancel out, or dissipate the coupling waves [14], [15], [16], [17], [37]. Nevertheless, these structures may impact the design's adaptability and the original beam pattern. It has been demonstrated that the RF isolation stage plays an important role in FD designs with more than 60 dB isolation achievable through various strategies [26].

In the related studies [12], [15], [16], [17], [26], [33], [35], [36], [37], however, most antenna isolation designs focus on a very limited number of antennas because of the challenges associated with simulation, manufacturing, and measurement. The experimental studies of Tx-to-Rx elements/sub-arrays between large-scale antenna arrays are still missing. Therefore, it is still essential to examine the antenna isolation approaches in large-scale array prototypes in order to discover potential opportunities, and advance the research and development of FD massive MIMO systems in practice. Our study potentially bridges this gap by designing and evaluating the antenna isolation between 64-Tx and 64-Rx elements with experimental measurements.

To effectively harness the advantages of a large-scale antenna array and its controllable beam pattern for SI mitigation, radio frequency (RF) beamformer design stands out as an essential component. In the context of FD communications within massive MIMO systems, several techniques and studies have come to the forefront [38], [39], [40], [41], [42]. A notable approach is the hybrid precoding/combining (HPC) technique for millimetre-wave (mmWave) FD massive MIMO systems, as detailed in [38]. This method employs angle-of-departure (AoD) and angle-of-arrival (AoA) data to diminish SI, while simultaneously reducing the number of RF chains. The research asserts that in point-to-point FD massive MIMO systems, the far-field and near-field SI channel powers are mitigated by 81.5 dB and 44.5 dB, respectively. In [39], separate and joint FD beamforming algorithms based on sequential convex programming are proposed to maximize the sumrate for both single-user (SU-) or multi-user (MU)-MIMO FD systems. In [40], an FD mmWave relaying system is considered to suppress SI while maximizing spectral efficiency using an orthogonal matching pursuit-based SI-cancellation algorithm. Similarly, an HPC design for FD amplify-and-forward (AF) mmWave relay systems is considered in [41], introducing a zero-space SI cancellation method based on correlated mmWave channel estimation errors. A distinct FD mmWave HBF strategy is introduced in [42] for MU-massive MIMO systems. This strategy formulates non-orthogonal beams to cater to multiple users, suppress the near-field element of the SI channel, and optimize sum-rate capacity. The study demonstrates that the proposed method can realize 78.1 dB of SIC in FD massive MIMO configurations.

While these existing SI suppression techniques in FD massive MIMO systems have demonstrated efficacy in mitigating strong SI from Tx to Rx and an isolation level of 78 dB to 81 dB can be achieved [38], [42], the performance evaluation primarily relies on theoretical SI channel models. For instance, studies [38], [39], [40], [41], [42] have based their assumptions on simulated residual near-field SI channels through line-of-sight (LoS) paths and far-field SI channels via reflected non-line-of-sight (NLoS) paths. However, a more realistic comprehension of beamforming-based SI suppression using measured SI channels is essential. Therefore, this research aims to provide an experimental evaluation of the beamforming-based SI suppression capability in FD massive MIMO system implementations.

### B. CONTRIBUTIONS

This work focuses on the development of a dual-layer metamaterial-based miniaturized large-scale array prototype capable of FD massive MIMO applications. Utilizing realistic simulations and experimental measurements, our goal is to present a comprehensive methodology for designing the FD massive MIMO antenna arrays and to showcase its potential in reducing the SI level via proper antenna isolation and beamforming design. To our knowledge, this is also the first work that investigates the far-field beam pattern and beam direction impacts on the FD isolation through experimental measurement results. The main contributions of this work are summarized as follows:

- **Miniaturized large-scale array prototype for FD massive MIMO:** We propose a cross-polarized, dual-layer metamaterial-based miniaturized large-scale array prototype. This antenna element structure achieves a notable size reduction of 65% by creating the slow-wave effect. Furthermore, we conduct a quantitative analysis of how the number of elements in the array influences its beam pattern. Theoretical expressions of the directivity and 3dB- and 10dB-beamwidth w.r.t. the number of elements in the array are derived. This provides insights into the effective length of the array in relation to directivity and beamwidth for large-scale array designs. We also explore the impact of the surrounding environment on the sub-array beam patterns using both HFSS simulations and experimental measurements. The effects of cross-polarization and separation distance on the Tx-to-Rx antenna element isolation are studied. Remarkably, an average isolation of 49.2 dB for Tx-to-Rx elements MC can be achieved across the two closest $4 \times 4$ sub-arrays.
- **Experimental studies of angular-perturbation beamforming isolation:** To further enhance the beam isolation, we investigate two RF beamformer design schemes, based on the angular locations of the users, which are as follows: 1) max-directivity-based RF beamformer; and 2) beam angle-perturbation-based RF beamformer. The first scheme enhances the Tx-to-Rx FD isolation by formulating the RF beamformers, which

maximize the power pattern peaks in the desired user directions. The second scheme introduces beam angle perturbations within 3dB-beamwidth of the desired beam angle to further enhance beam isolation in FD massive MIMO. Experimental measurements are conducted to evaluate the beam isolation performance. Average beam isolation of 65.6 dB and the highest isolation level of 79.6 dB can be achieved between the sample $1 \times 4$ Tx/Rx sub-arrays with the second scheme, which shows an average 16.4 dB isolation improvement.

- **The correlation between far-field pattern and beam isolation:** Experimental measurements of far-field beam patterns have been conducted to elucidate their influence on the beam isolation level. Our findings indicate that substantial beam level isolation can be attained when the Rx beams are aligned with the radiation nulls of the Tx beams. The results can offer valuable insights for angular-based or arbitrary radiation-nulling-based FD beamforming isolation design.

### C. ORGANIZATION

The rest of the paper is structured as follows. Section II delves into the design process of the antenna elements and the $8 \times 8$Tx/$8 \times 8$Rx FD massive MIMO array prototype. Section III provides a detailed investigation of the antenna element radiation patterns, circular-polarization axial ratios (AR), and Tx/Rx MC characteristics. This section also investigates potential changes in the sub-array beam pattern when positioned at different locations on a large array. It further explores the variation in the linear antenna array radiation pattern with the number of elements change, given different element pattern assumptions. Section IV introduces the system model employed for beam-level isolation design. Additionally, two distinct beamformer designs are presented. Section V offers empirical results from the experimental measurements conducted on the FD massive MIMO prototype, alongside optimization techniques for beam-level isolation. Section VI concludes the paper and provides possible future works.

### D. NOTATION AND COORDINATES

In the presentation, the antenna array is placed in the $xy$ plane and the main radiation direction is perpendicular to the array plane (along the $z$-axis) and is defined as $\theta = 0°$ and $\phi = 0°$. Therefore, the $\theta$ angle plane is the $xz$ plane. The analysis calculates all the averages in the decimal values first and then transfers them into the decibel (dB) scale. The following notations are used throughout this paper. Boldface lower-case and upper-case letters denote column vectors and matrices, respectively. $()^T$, $()^H$ and $\|.\|$ represent the transpose, complex-transpose, and the 2-norm of a vector or matrix, respectively. $\mathbf{I}_k$, [.] and (.) denote $k \times k$ identity matrix, the expectation operator and the trace operator, respectively. We use $x_k \sim \mathcal{CN}(0, \sigma^2)$ when $x_k$ is a complex Gaussian random variable with zero-mean and variance $\sigma^2$.

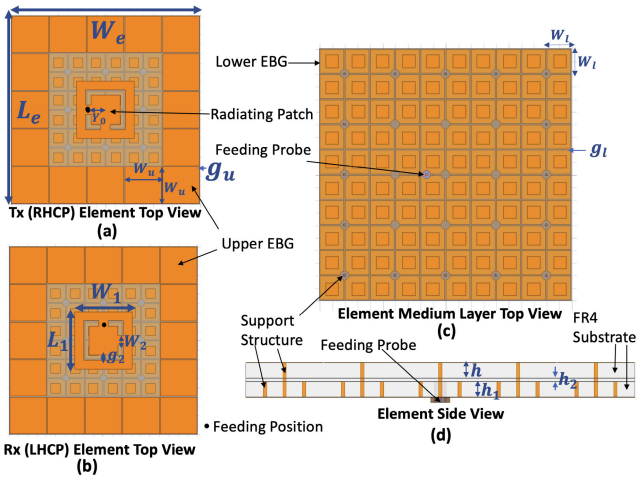


**FIGURE 1.** (a) Tx antenna top view; (b) Rx antenna top view; (c) top view of the element medium layer; (d) side view of the multi-layer structure.

**TABLE 1.** Parameters of the proposed antenna element.

| Parameter | Description | Value (mm) |
|---|---|---|
| $W_e$ | element width | 40 |
| $L_e$ | element length | 40 |
| $W_1$ | patch width | 12.2 |
| $L_1$ | patch length | 12.2 |
| $W_2$ | bridge width | 2.0 |
| $Y_0$ | feeding point from the center | 3.0 |
| $g_u$ | upper EBG gap | 0.2 |
| $g_l$ | lower EBG gap | 0.2 |
| $g_2$ | center patch slot gap | 1.1 |
| $W_l$ | lower EBG size | 3.8 |
| $W_u$ | upper EBG size | 7.8 |
| $h$ | upper FR-4 substrate thickness | 1.6 |
| $h_1$ | lower FR-4 substrate thickness | 1.6 |
| $h_2$ | prepreg thickness | 0.2 |

## II. RECTANGULAR ANTENNA ARRAYS FOR FD MASSIVE MIMO

### A. DUAL-LAYER EBG MINIATURIZED ANTENNA ELEMENT STRUCTURE

The proposed FD massive MIMO arrays consist of dual-layer electromagnetic-bandgap (EBG) slotted antenna elements [43], which operate within the 3.35 GHz to 3.6 GHz frequency band. The structures of the Tx and Rx antenna elements are depicted in Fig. 1. The Ansoft ANSYS High-Frequency Structural Simulator (HFSS) Eigen Solver and Optimetrics Analyzer are used to calculate and optimize the structure dimensions, as shown in Table 1. The dual-layer design introduces the near-field coupling and reflection interference between the upper and lower patches, leading to a variation in both the wave reflection phase and the dispersion relationship [44]. When the incident and reflected waves converge with constructive interference, the phase velocity of the wave traversing through the structure is slower than its phase velocity in free space. By adjusting the sizes and gaps between the top and bottom patches, the waves operate in a slow-wave domain, marked by this

decreased phase velocity. As a result, a scaled-down effective wavelength ($\lambda_{eff}$) can be realized, leading to the possibility of reducing the antenna size. The relationship between the $\lambda_{eff}$ and the relative size of the two-layer square patches can be found as [32]

$$\lambda_{eff} = \frac{\lambda_0(W_l + g_l)}{W_u}, \tag{1}$$

where $\lambda_0$ is the free-space wavelength at the target operating frequency ($\lambda_0 = 8.6$ cm, at 3.5 GHz) and $W_u$ is the width of the upper layer EBG cell. $W_l$ is the width of the lower square EBG patches, and $g_l$ is the gap length between two neighbouring lower EBG patches. The conventional half-wavelength patch antenna on FR-4 PCB material at 3.5 GHz would be 20.5 mm ×20.5 mm. With the lower-layer EBG structure, the dimension of the center radiating patch can be reduced to 12.2 mm × 12.2 mm, which is about 40% reduction per side and 65% area reduction.

The conventional microstrip patch antenna suffers from strong wave leakage along the dielectric substrates. The proximity of antenna elements can result in strong inter-element MC, which can have detrimental effects on radiation efficiency and distort the radiation pattern. The small radiating patch leaves extra space for the additional upper-layer miniaturized EBG structure, which creates a high surface impedance and works as a band-stop filter for the surface coupling waves. The introduction of this periodic lattice structure enhances the inter-element isolation within the array. As illustrated in [45], the relationship between the theoretical surface impedance ($Z_S$) and dimensions of the upper-layer EBG structure is given as

$$C = \frac{W_u\epsilon_0(1+\epsilon_r)}{\pi}\cosh^{-1}\left(\frac{W_u + g_u}{g_u}\right), \quad L = \mu h,$$
$$Z_S = \frac{j\omega L}{1-\omega^2 LC}, \tag{2}$$

where $g_u$ is the gap width between neighbouring upper EBG patches and $h$ is the substrate thickness. $\epsilon_r$ is the dielectric constant of the substrate. The gap between the conducting surface can create the edge capacitance ($C$), and the current, along with the adjacent cells, will generate the inductance ($L$). The simulation and measurements of the proposed EBG structure and the antenna element are shown in [43]. With the proposed square EBG structure, a surface impedance exceeding 4000Ω can be achieved at 3.5 GHz. In the band 3.35 to 3.6 GHz, the return loss of all the elements is better than 10 dB, and the MC between neighbouring elements in all directions is lower (better) than −14.3 dB at a radiating patch separation distance of 2.78 cm ($0.32\lambda_0$) edge-to-edge.

Circular polarization (CP) is employed in the proposed patch antenna structure. To improve the isolation in the FD communications, the Tx and Rx antennas have been cross-polarized. However, the inherent challenges of microstrip patch antennas, due to their planar structure and excitation of multiple modes, mean that achieving optimal circular polarization performance can be challenging. To get a pure

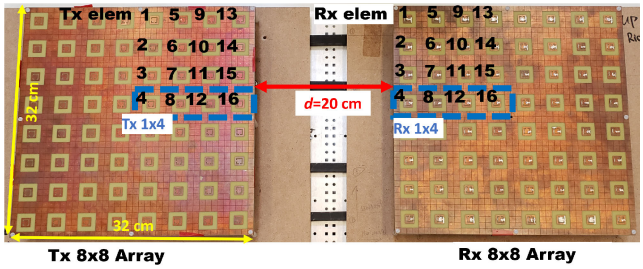


**FIGURE 2.** Antenna array prototype for FD massive MIMO and indices of sample sub-arrays and elements used in the measurement.

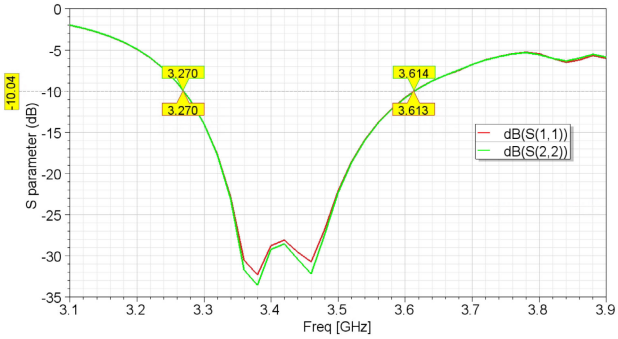


**FIGURE 3.** Return loss of Tx element (labelled by S(1,1)) and Rx element (labelled by S(2,2)) (simulation results).

CP and maximize the polarization mismatch, intricate feeding circuits are usually implemented to generate orthogonal polarization and manage the CP direction. However, this approach leads to high hardware complexity and challenges in feeding line management in the massive array design. To simplify the feeding structure in the proposed multi-layer structure, we control the states of CP through the relative positioning of the feeding point and the directions of slots on the central radiating patch. A single feeding probe is positioned 3 mm from the center of the patch element. Specifically, the transmitting (Tx) elements are tailored to get right-handed circular polarization (RHCP). Conversely, the receiving (Rx) elements, created by mirroring the Tx radiating patch, produce left-handed circular polarization (LHCP), as illustrated in Fig. 1 (a) and (b).

### B. CROSS-POLARIZED 8 × 8 ANTENNA-ARRAY PROTOTYPES

In the design of the Tx/Rx antenna array, avoiding the spatial aliasing effect is crucial. This effect can arise when the separation distance between elements surpasses half a wavelength. The consequence is a coherent addition of plane waves with different incident angles, leading to grating lobes. These grating lobes not only degrade beam resolution but can also introduce significant interference. To circumvent this issue in our design, the separation distance between neighbouring elements is set to 2.78 cm ($0.32\lambda_0$ at 3.5 GHz) edge-to-edge or 4.00 cm ($0.47\lambda_0$) center-to-center. All elements share the same FR4 dielectric substrate and the ground plane. Each array dimensions to a width of

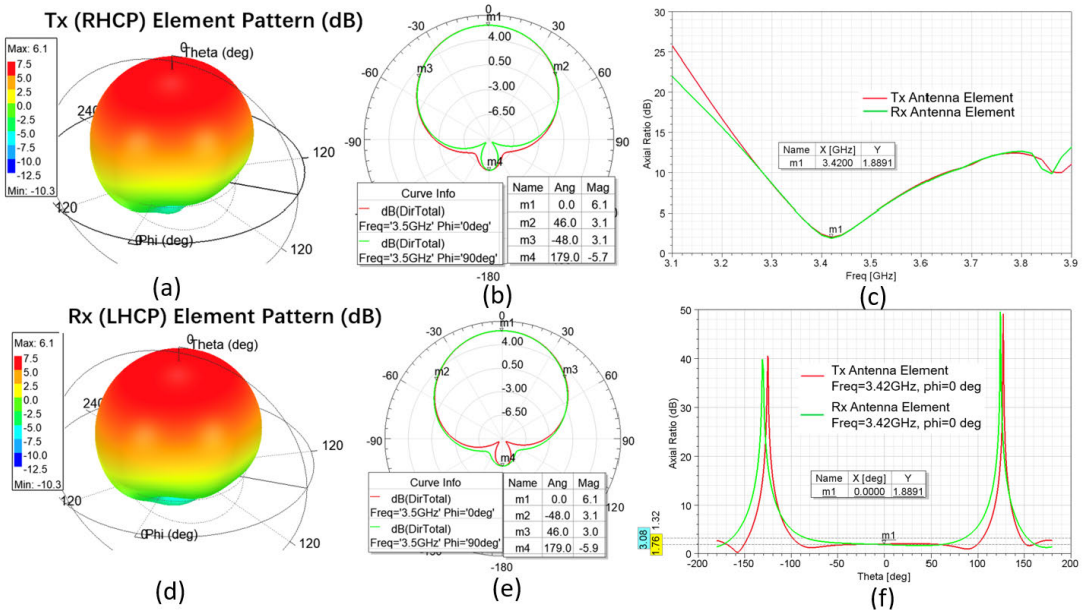


**FIGURE 4.** Element radiation patterns (directivity in dB) and element AR, (a) Tx element 3D at 3.5 GHz, (b) Tx 2D cut at $\phi = 0°, 90°$ at 3.5 GHz, (c) Tx/Rx AR (dB) versus operating frequency (GHz), (d) Rx element 3D at 3.5 GHz, (e) Rx 2D cut at $\phi = 0°, 90°$, (f) Tx/Rx AR at 3.42 GHz (simulation results).

$W_T = 32$ cm and a length of $L_T = 32$ cm. The structure of the $8 \times 8$Tx/$8 \times 8$Rx antenna array prototype for FD massive MIMO is illustrated in Fig. 2. The two arrays are spaced apart by $d = 20$ cm. Taking this separation into account, the entire Tx-Rx antenna-array set measures 84 cm in length and 32 cm in width, accommodating a total of 64 transmitting and 64 receiving elements.

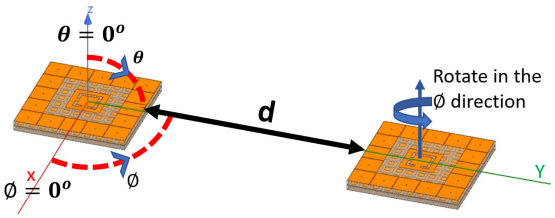


**FIGURE 5.** Locations of Tx and Rx elements in the MC simulation.

## III. ANTENNA CHARACTERISTICS

### A. ELEMENT RADIATION CHARACTERISTICS

#### 1) ELEMENT RETURN LOSS AND IMPEDANCE BANDWIDTH

The HFSS simulated S-parameters, which illustrate the impedance match bandwidth of the proposed Tx and Rx antenna elements are presented in Fig. 3. Both the Tx and Rx elements achieve a return loss better than 10 dB within the band 3.27 GHz to 3.61 GHz, which indicates an effective impedance match bandwidth of 340 MHz or 9.7% at 3.5 GHz. The return loss is better than 20 dB within the band 3.33 GHz to 3.51 GHz.

#### 2) ELEMENT RADIATION PATTERN AND BEAMWIDTH

The simulated radiation patterns for the Tx (RHCP) and Rx (LHCP) antenna elements are depicted in Fig. 4. Both elements display symmetric radiation patterns, each with a directivity of 6.1 dB. The realized gains for the Tx and Rx elements stand at 5.1 dB and 5.2 dB, respectively, corresponding to radiation efficiencies of 79.4% for the Tx and 81.3% for the Rx. The 3dB-beamwidth is around 94° in both directions $\phi = 0°$ and $\phi = 90°$. The normalized front-to-back ratios of the Tx and Rx elements, which quantify the power difference between the forward and backward radiation, are $-11.8$ dB and $-12$ dB, respectively. Notably, the Rx element's radiation pattern can be derived by rotating the Tx element pattern by 90° in the $\phi$ plane.

#### 3) ANTENNA-ELEMENT CIRCULAR-POLARIZATION AXIAL RATIO

The AR simulation results at different operating frequencies of the proposed Tx and Rx antenna elements are presented in Fig. 4 (c). It can be observed that the best AR of 1.9 dB can be achieved at 3.42 GHz. The Tx/Rx antenna element AR in the $\theta$ angle range at 3.42 GHz is illustrated in Fig. 4 (f). The results show that the Tx/Rx elements achieve an AR better than 3 dB in the whole front radiation range, i.e., from $-90°$ to 90°. However, we observe in Fig. 4 (c) that the antenna AR performance is sensitive to the operating frequency. More details on the sub-array AR in the beamforming process will be presented in Section V-B.

### B. ANTENNA-ELEMENT TX-TO-RX MUTUAL COUPLING SIMULATION

The MC between Tx and Rx antennas is influenced by both the separation distance ($d$) and polarization efficiency.

**TABLE 2.** MC between tx and rx antenna vs separation distance ($d$) at 3.5 GHz (dB).

| | Separation d (cm) | 0 | 4 | 8 | 12 | 16 | 20 |
|---|---|---|---|---|---|---|---|
| 1 | $\phi = 0^o$ | -15.2 | -28.4 | -32.7 | -35.7 | -37.8 | -39.6 |
| 2 | $\phi = 90^o$ | -14.5 | -28.5 | -32.5 | -35.1 | -37.2 | -38.9 |
| 3 | $\phi = 180^o$ | -15.4 | -28.7 | -33.2 | -36.2 | -38.3 | -40.2 |
| 4 | $\phi = 270^o$ | -15.9 | -29.6 | -33.5 | -36.1 | -38.3 | -39.9 |
| 5 | Mirrored (OP) | -24.2 | -36.3 | -42.3 | -46.1 | -48.39 | -51.3 |

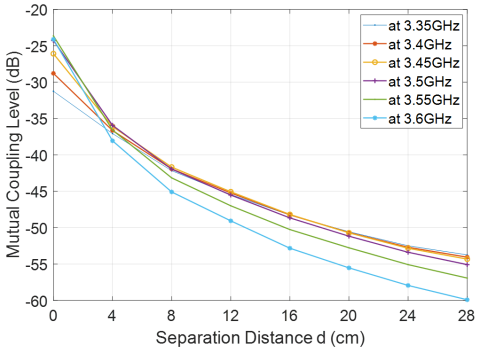


**FIGURE 6.** Tx-to-Rx MC magnitude vs separation distance (operating frequency from 3.35 to 3.6 GHz).

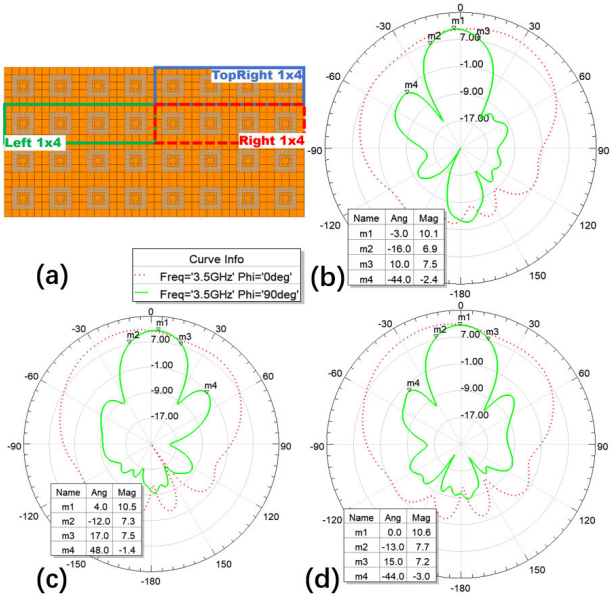


**FIGURE 7.** 1 × 4 sub-arrays on a 4 × 8 array: sub-array locations (a) and $\phi = 0°$ and $\phi = 90°$ 2D cuts beam pattern at steering angle $\theta = 0°$ of TopRight 1 × 4 (b), Left 1 × 4 (c), and Right 1 × 4 (d) (simulation results).

A series of simulations are conducted to understand the interplay between separation and MC, as well as the effects of cross-polarization. As shown in Fig. 5, the simulation begins with both the Tx and Rx antennas having identical polarization and being aligned in the same direction (both RHCP, $\phi = 0°$). In subsequent trials, the Rx antenna's orientation is rotated by increments of 90° within the $\phi$ plane. The edge-to-edge separation $d$ is increased in increments of 4 cm, ranging from 0 cm to 20 cm. Additionally, the Rx antenna is also mirrored in the simulation, where the polarization status of the Rx antenna is changed to LHCP. The results are shown in Table 2.

#### 1) TX-TO-RX MC VERSUS POLARIZATION STATES

The observations made regarding the MC levels in the first four configurations ($\phi$ from 0° to 270°) are less than 1.4 dB. This fact indicates that when both Tx and Rx antennas have the same polarization states, the rotation of the Rx element cannot successfully reduce the MC level. A considerable improvement in isolation can be seen when Tx and Rx antenna elements are placed in a mirrored configuration, where the Tx antenna is RHCP, and the Rx antenna is LHCP. Compared to the average MC magnitude of the first four configurations, the orthogonal polarization configurations yield an average 8.9 dB lower (better) MC level. The improvement in isolation varies, with a maximum of 11.7 dB lower (better) MC at a 20 cm separation and a minimum of 7.5 dB lower MC at a 4 cm separation. As a result, Configuration 5 is used in our design and the rest of the simulations and measurements.

#### 2) TX-TO-RX MC VERSUS SEPARATION DISTANCE

The MC versus Tx-to-Rx element separation distance simulation results for the entire target range from 3.35 GHz to 3.60 GHz are plotted in Fig. 6. All six curves follow a similar trend. Beyond a separation distance of 20 cm ($d = 2.5\lambda_0$), the curve slope begins to flatten, indicating a reduced rate of decrease in the MC magnitude. Further increasing the separation distance by 8 cm, the decrease of the MC magnitude is less than 5 dB. These observations suggest that as the separation distance surpasses 20 cm, the impact of the line-of-sight (LOS) path near-field coupling wave diminishes. The far-field component becomes the dominant factor in determining the overall MC level when $d \geq 3\lambda_0$.

Two sample 4 × 4 antenna arrays with the intended Tx and Rx antenna elements separated by 20 cm edge-to-edge are simulated in HFSS to further explore the MC between elements in antenna arrays. The results show an average MC level of −48.4 dB across 256 Tx-to-Rx element pairs at 3.5 GHz, which is 2.9 dB higher than the result when only two elements are used in the simulation. When the edge-to-edge separation of the two 4 × 4 arrays is extended to 24 cm, the average Tx-to-Rx element MC is reduced at −49.5 dB, which is 1.1 dB less than the average MC observed at $d = 20$ cm. Hence, we select $d = 20$ cm as the separation distance between the Tx and Rx arrays, striking a balance between isolation performance and the overall dimensions of the structure.

### C. ANTENNA SUB-ARRAY BEAMFORMING

The far-field radiation pattern of M-antenna-element array beamforming can be represented as

$$z(\theta, \phi, r) = \frac{e^{-jkr}}{r} \sum_{m=0}^{M-1} w_m^* A_m f_m(\theta, \phi) e^{-jk(\mathbf{u}\cdot\mathbf{x_m})}, \quad (3)$$

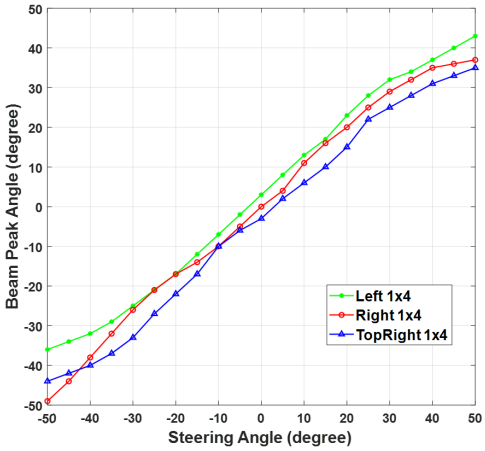


**FIGURE 8.** Sub-array beam peak angle vs target steering angle (simulation results).

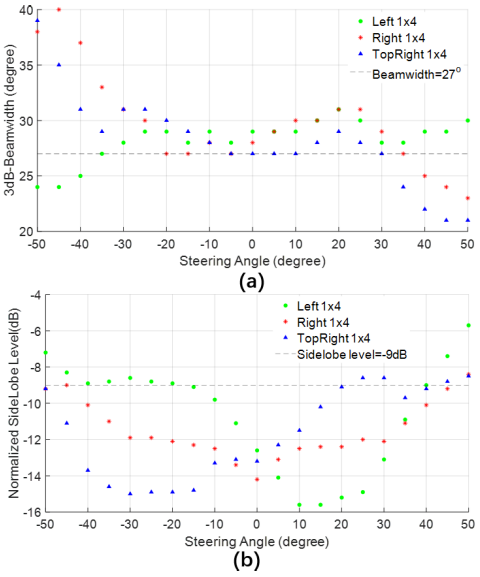


**FIGURE 9.** 3dB-Beamwidth and normalized sidelobe levels of 1 × 4 sub-arrays for steering angle from −50° to 50° (simulation results).

where $k$ is the phase constant and equals to $2\pi/\lambda_0$. $r$ is the distance between the far-field observation point and the origin of the antenna array. $A_m$ is the gain, and $f_m(\theta, \phi)$ is the normalized radiation pattern of the $m$th antenna element, representing the angular distributions of the electromagnetic field created by the $m$th element. $\mathbf{x_m}$ is the position vector of the $m$th element, and $\mathbf{u}$ is the unit directional vector from the array origin to the far-field observation point. $w_m$ is a complex steering weight for the $m$th element. The equation illustrates that when individual antenna elements are aggregated into arrays, the beam radiation pattern can be impacted by the element patterns and the geometry layout of the elements.

### 1) SIMULATION OF SUB-ARRAY BEAMFORMING

#### *a: SIMULATION SETUP*

The proposed antenna element is designed with a dual-layer rectangular EBG structure. This intricate design inherently demands high computational resources for accurate and realistic simulations. Due to the limitation of the computation resources, especially the RAM, (available PC with 640GB RAM and 70 CPU cores), the HFSS simulation of the complete 8 × 8 array with the proposed element structure is challenging. Therefore, a 4 × 8 antenna array consisting of the proposed RHCP elements is simulated to examine how the sub-array beamforming performance changes at different locations on a large array. For a comparative analysis, three sample 1 × 4 sub-arrays located in the left, right, and right-top edges are chosen, as illustrated in Fig. 7(a). The beams are steering within a $\theta$ angle from −50° to 50°, adjusted in increments of 5°. The steering weights used in the simulations have a uniform magnitude, and phase shift values are changed based on the steering angle.

#### *b: SIMULATION RESULTS*

The simulated 2D cuts at $\phi = 0°$ and $\phi = 90°$ of three sub-arrays at steering angle $\theta = 0°$ are shown in Fig. 7. Positioned in the array's top two rows, these sub-arrays produce beams with noticeable downward tilts, as evidenced in the $\phi = 0°$ cut plots. The Left 1 × 4 sub-array exhibits a beam tilted by 4°, while the TopRight 1 × 4 sub-array has a beam tilted by −3° in the $\theta$ angle. Notably, all three beams maintain a normalized sidelobe level below −11.9 dB. The Right 1 × 4 sub-array demonstrates a 1.1 dB lower normalized sidelobe level compared to the TopRight 1 × 4 sub-array situated at the edge.

*Sub-array Directivity Variation:* Within a $\theta$ steering range −50° to 50°, the average directivity for the Left, Right, and TopRight 1 × 4 sub-arrays are 11.2 dB, 11.2 dB, and 10.9 dB, respectively, demonstrating that location variation has a negligible effect on beamforming directivity.

*Sub-array Location vs Beam Peak Tilted:* Fig. 8 depicts the beam peak directions achieved by the three sub-arrays relative to the intended steering angle. Notably, the Left 1 × 4 sub-array plot consistently exhibits a higher position compared to the results of the Right and TopRight sub-arrays. With identical steering weights, the Left 1 × 4 sub-arrays get a beam steering angle of 3.5° greater compared with the Right sub-array on average. The TopRight 1 × 4 sub-array has an average difference of −3°, in comparison to the Right sub-array.

Moreover, it can be observed that a larger beam peak tilt occurs when the beam is steering away from the array center. For the Left 1 × 4 sub-array, an average angle tilt of 5.7° is observed when steering within the range $\theta = -50°$ to $\theta = 0°$. In contrast, the Right 1 × 4 and TopRight 1 × 4 sub-arrays display average beam tilts of −2.7° and −6.5°, respectively, when steering within the range $\theta = 0°$ to $\theta = 50°$. This trend indicates that the beam tilt angle increases as the steering angle moves further away from the array center. Consequently, the following observations can be made: 1) Asymmetrically positioned sub-arrays tend to tilt

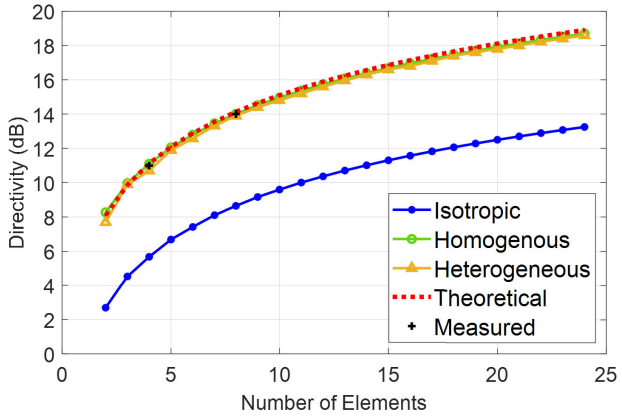


**FIGURE 10.** Linear array directivity vs number of antenna elements.

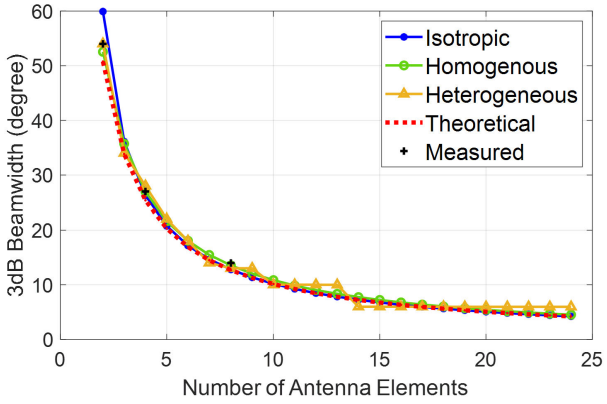


**FIGURE 11.** 3dB-beamwidth vs number of antenna elements.

their beams towards the array's center. The beam tilt gets larger as the steering angle increases; 2) Edge sub-arrays demonstrate radiation patterns more titled towards the array center compared with the sub-arrays close to the array center.

*Sub-array Location vs Sidelobe and Beamwidth:* The simulation results of the 3dB-beamwidth and the normalized sidelobe level w.r.t. the main beam peak of the three sub-arrays across $\theta$ steering range $-50°$ to $50°$ are shown in Fig. 9.

When steering away from the array centre, the sub-arrays with asymmetric placements get a relatively narrower 3dB-beamwidth. Additionally, Fig. 9(b) illustrates that the sub-arrays with an asymmetric position typically exhibit quicker sidelobe level increases while steering away from the array centre and the edge sub-array sidelobe level grows more quickly than the centre sub-array sidelobe. The high sidelobe levels can potentially increase interference with other signals or systems operating in the sidelobe regions and also lead to a loss of signal power in the main lobe directions, leading to a degradation in the beamforming performance.

The presence of the ground plane and EBG patches acts as a reflective medium, leading to reflections and interference with the direct radiation from the patch elements.

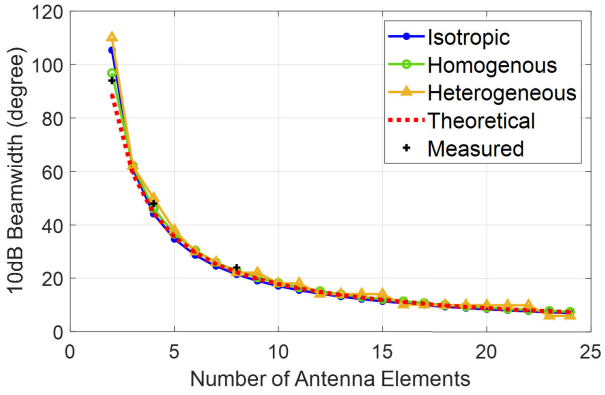


**FIGURE 12.** 10dB-beamwidth vs number of antenna elements.

Therefore, when a sub-array is asymmetrically positioned on the array during the beamforming process, this non-uniform reflecting surface contributes to an extra amount of radiation interference. There is an amplified radiation on the side with a larger reflective surface. Therefore, the main lobe pattern becomes asymmetric and the radiation intensity is more pronounced in the direction of the larger ground plane, leading to the beam angle tilt. When the beam steers towards the array center (where the ground plane is larger), the extra reflection adds into the main lobe and contributes to a wider beamwidth. Meanwhile, when steering the beam away from the array center, the extra reflected waves become a main contributor to the sidelobe level increase.

### D. LINEAR ARRAY BEAM PATTERN AND THE NUMBER OF ELEMENTS

In this section, we delve into an analysis of how the linear array beam pattern shifts as the number of elements grows. Understanding these variations equips designers with insights to determine an effective array size in the beamforming and to assess the impact of the element pattern on the array beam. To provide a comprehensive analysis, we derive theoretical expressions for the array beam directivity and beamwidth. Three simulation scenarios are used to compare with the theoretically estimated values, which are: 1) *isotropic* with all elements assumed to be isotropic; 2) *homogeneous* with all elements assumed to have the identical isolated Tx patch element radiation pattern; 3) *heterogeneous* with each element having a different radiation pattern from the HFSS simulation. Elements in the simulation are spaced apart by a half-wavelength (4 cm). Illustrative results show that the theoretical expressions can estimate the directivity and beamwidth values accurately. Notably, as the number of antenna elements grows, the linear array's main beam pattern becomes progressively less influenced by individual element patterns.

#### 1) DIRECTIVITY VS NUMBER OF ANTENNA ELEMENTS

In the context of a uniformly excited linear array comprising M-elements equally spaced at a half-wavelength distance the

theoretical directivity ($D$) can be articulated as

$$D[dB] = D_{elem}[dB] + 10log_{10}(M), \tag{4}$$

where $D_{elem}$ is the single element directivity used in the array, and in our simulation, $D_{elem} = 6.1$ dB. The comparison between the theoretical values and the simulated results is shown in Fig. 10. It is notable that all three plotted curves echo similar trajectories. The average and maximum difference between homogeneous, heterogeneous, and theoretical values are, respectively, less than 0.3 dB and 0.6 dB, which shows that the theoretical equation can estimate the heterogeneous case accurately. Additionally, the average difference between the isotropic array and heterogeneous results is 5.3 dB, where the difference mainly comes from the 6.1 dB directivity difference between the proposed element and the isotropic element. The measured results of $1 \times M$ sub-arrays for $M =$ 4,8, are in close agreement with the simulation results, with an average difference within 0.5 dB. Further details on measured results are discussed in Section V.

#### 2) BEAMWIDTH VS NUMBER OF ANTENNA ELEMENTS

For a uniformly excited, equally half-wavelength spaced M-element linear isotropic array, the far-field radiation pattern can be represented as

$$\begin{aligned} z_i(\theta, \phi, r) &= \frac{e^{-jkr}}{r} \sum_{m=0}^{M-1} e^{-jm\pi cos(\theta)} \\ &= \frac{e^{-jkr}}{r} e^{-j(M-1)\pi cos(\theta)/2} \frac{sin(M\pi cos(\theta)/2)}{sin(\pi cos(\theta)/2)}. \end{aligned} \tag{5}$$

As a result, the AdB-beamwidth is $2\theta_{AdB}$, where $\theta_{AdB}$ is the $\theta$ solution of the following equation

$$\frac{sin(M\pi cos(\theta)/2)}{sin(\pi cos(\theta)/2)} = 10^{\frac{-A_{dB}}{10}}. \tag{6}$$

For $M \gg 2$, the 3dB- and 10dB-beamwidths in radians can be derived as

$$BW_{3dB} = \frac{1.77}{M}, \quad BW_{10dB} = \frac{1.55}{M}, \tag{7}$$

i.e., they are inversely proportional to the number of elements.

For the 3dB-beamwidth, Fig. 11 shows that all cases follow a similar trend. As the number of elements increases, the difference between all scenarios diminishes. Notably, when $M > 2$, differences among the simulation cases become less than 2°. This gap narrows to under 1° when $M > 10$. Similar observations can be found in the 10dB-beamwidth simulation results, as shown in Fig. 12. When $M > 4$, the difference in 10dB-beamwidth across the three simulation setups is less than 5°. The experimentally measured results of $1 \times M$ sub-arrays are in close agreement with simulation results, with an average difference less than 1°, when $M = 4, 8$.

As the number of elements increases, the element pattern effects on the array main lobe pattern become negligible. The beamwidth decrease rate becomes slow when $M \geq 8$ and becomes nearly flat when $M > 14$, where the 3dB- and 10dB-beamwidths become smaller than 7° and 14°, respectively.

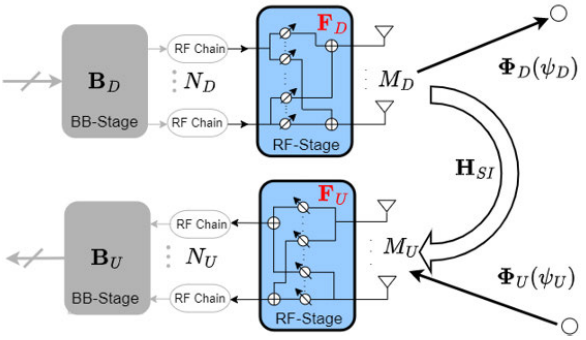


**FIGURE 13.** System model of proposed FD massive MIMO.

## IV. RF BEAMFORMING-BASED ENHANCED ISOLATION

To further improve the isolation in the FD massive MIMO operation, it is important to consider beamforming design for mitigating the strong SI. Beamforming concentrates the radiation power in the intended direction and reduces the transmitting leakage wave between the Tx and the local Rx, and improves the spatial separation in the FD operation [46]. Steering the directional beams towards the radiation nulls of the undesirable interference source considerably reduces far-field interference. In the rest of this section, we first discuss the system model of FD massive MIMO system followed by the problem formulation and the proposed two beamforming techniques for enhanced isolation.

### A. SYSTEM MODEL

We consider a single-cell FD massive MIMO system for joint downlink (DL) and uplink (UL) transmission as shown in Fig. 13. Here, the BS operates in FD mode to simultaneously serve $K_D$ DL and $K_U$ UL single-antenna users over the same frequency band, while the users operate in HD mode due to the hardware/software constraints (e.g., low power consumption, limited signal processing, and active/passive SIC capability). As shown in Fig. 2, both Tx and Rx are equipped with uniform rectangular arrays (URAs), which are separated by an antenna isolation block for passive (i.e., propagation domain) SI suppression. A 20MHz modulated signal in the band 3.49 GHz to 3.51 GHz is transmitted in the experiments to measure the beam MC in an anechoic chamber. The details of the measurement setup in the anechoic chamber are discussed in Section V. The transmit (receive) URA has $M_D = M_D^{(x)} \times M_D^{(y)} (M_U = M_U^{(x)} \times M_U^{(y)})$ antennas, where $M_D^{(x)}(M_U^{(x)})$ and $M_D^{(y)}(M_U^{(y)})$ denote the number of transmit (receive) antennas along $x$-axis and $y$-axis, respectively. For the proposed FD massive MIMO system, we consider the DL signal is processed through DL baseband (BB) stage $\mathbf{B}_D \in \mathbb{C}^{N_D \times K_D}$ and DL RF beamformer $\mathbf{F}_D \in \mathbb{C}^{M_D \times N_D}$, where $N_D$ is the number of RF chains such that $K_D \leq N_D \ll M_D$. Similarly, the received UL signal at BS is processed through UL RF beamformer $\mathbf{F}_U \in \mathbb{C}^{N_U \times M_U}$ and UL BB combiner $\mathbf{B}_U \in \mathbb{C}^{K_U \times N_U}$ by utilizing $K_U \leq N_U \ll M_U$ RF chains. Here, the UL

and DL RF beamforming stages (i.e., $\mathbf{F}_U$ and $\mathbf{F}_D$) are built using low-cost phase-shifters (PSs). The DL channel matrix is denoted as $\mathbf{H}_D = [\mathbf{h}_{D,1}, \cdots, \mathbf{h}_{D,K_D}]^T \in \mathbb{C}^{K_D \times M_D}$ with $\mathbf{h}_{D,k} \in \mathbb{C}^{M_D}$ as the $k^{th}$ DL UE channel vector. Similarly, $\mathbf{H}_U = [\mathbf{h}_{U,1}, \cdots, \mathbf{h}_{U,K_U}] \in \mathbb{C}^{M_U \times K_U}$ is the UL channel matrix with $\mathbf{h}_{U,k} \in \mathbb{C}^{M_U}$ as the $k^{th}$ UL UE channel vector. Due to the FD transmission, the SI channel matrix $\mathbf{H}_{SI} \in \mathbb{C}^{M_U \times M_D}$ is present between Tx and Rx antennas at the BS. For the DL transmission, the transmitted signal vector at the BS is defined as $\mathbf{s}_D = \mathbf{F}_D\mathbf{B}_D\mathbf{d}_D \in \mathbb{C}^{M_D}$, where $\mathbf{d}_D = \left[d_{D,1}, \cdots, d_{D,K_D}\right]^T \in \mathbb{C}^{K_D}$ is the DL data signal vector such that $\{\mathbf{d}_D\mathbf{d}_D^H\} = \mathbf{I}_{K_D}$. The transmitted signal vector satisfies the maximum DL transmit power constraint, which is $\{||\mathbf{s}_D||^2\} = (\mathbf{F}_D\mathbf{B}_D\mathbf{B}_D^H\mathbf{F}_D^H) \leq P_D$, where $P_D$ is the total DL transmit power. Then, the received DL signal vector is given as follows:

$$\mathbf{r}_D = \underbrace{\mathbf{H}_D\mathbf{F}_D\mathbf{B}_D\mathbf{d}_D}_{\text{Desired Signal}} + \underbrace{\mathbf{H}_U\mathbf{d}_U}_{\text{IUI by UL UE}} + \underbrace{\mathbf{n}_D}_{\text{Noise}}, \tag{8}$$

where $\mathbf{H}_U \in \mathbb{C}^{K_D \times K_U}$ is the inter-user interference (IUI) between the DL/UL UE and $\mathbf{n}_D = \left[n_{D,1}, \cdots, n_{D,K_D}\right]^T \sim \mathcal{CN}\left(0, \sigma_n^2\mathbf{I}_{K_D}\right)$ is the complex circularly symmetric Gaussian noise vector. Here, we define $P_U$ as the transmit power of each UL UE. Similar to the DL data signal vector, the UL received signal at BS can be written as follows:

$$\tilde{\mathbf{r}}_U = \underbrace{\mathbf{B}_U\mathbf{F}_U\mathbf{H}_U\mathbf{d}_U}_{\text{Desired Signal}} + \underbrace{\mathbf{B}_U\mathbf{F}_U\mathbf{H}_{SI}\mathbf{F}_D\mathbf{B}_D\mathbf{d}_D}_{\text{SI}} + \underbrace{\tilde{\mathbf{n}}_U}_{\text{Modified Noise}}, \tag{9}$$

where $\mathbf{d}_U = \left[d_{U,1}, \cdots, d_{U,K_U}\right]^T \in \mathbb{C}^{K_U}$ is the UL data signal vector such that $\mathrm{E}\left\{\mathbf{d}_U\mathbf{d}_U^H\right\} = \mathbf{I}_{K_U}$ and $\tilde{\mathbf{w}}_U = \mathbf{B}_U\mathbf{F}_U\mathbf{w}_U$, where $\mathbf{n}_U = \left[n_{u,1}, \cdots, n_{U,K_U}\right]^T \sim \mathcal{CN}(0, \sigma_n^2\mathbf{I}_{K_U})$ is the complex circularly symmetric Gaussian noise vector. The desirable DL (UL) beam direction has azimuth and elevation angles $\theta_D(\theta_U)$ and $\psi_D(\psi_U)$, respectively. For simplicity, we consider the FD BS serves a single UL and a single DL UE (i.e., $K_D = K_U = 1$)[1]; and 2) fixed DL/UL elevation angles $\psi_D = \psi_U = 90°$. Then, the phase response vectors of the DL and UL directions can be written as follows:

$$\Phi_D(\theta_D) = [1, e^{-j2\pi d\cos(\theta_D)}, \cdots, e^{-j2\pi d(M_D-1)\cos(\theta_D)}]^T \in \mathbb{C}^{M_D \times 1}, \tag{10}$$

$$\Phi_U(\theta_U) = [1, e^{j2\pi d\cos(\theta_U)}, \cdots, e^{j2\pi d(M_U-1)\cos(\theta_U)}]^T \in \mathbb{C}^{M_U \times 1}. \tag{11}$$

Let $\hat{\theta}_D$ and $\hat{\theta}_U$ are the beamsteering azimuth angles of the Tx and Rx beams, respectively. Then, the Tx and Rx RF beamformers (beamsteering vectors) can be written as follows:

$$\mathbf{f}_D(\hat{\theta}_D) = \frac{1}{\sqrt{M_D}}[1, e^{j2\pi d\cos(\hat{\theta}_D)}, \cdots, e^{j2\pi d(M_D-1)\cos(\hat{\theta}_D)}]^T \in \mathbb{C}^{M_D \times 1}, \tag{12}$$

$$\mathbf{f}_U(\hat{\theta}_U) = \frac{1}{\sqrt{M_U}}[1, e^{-j2\pi d\cos(\hat{\theta}_U)}, \cdots, e^{-j2\pi d(M_U-1)\cos(\hat{\theta}_U)}]^T \in \mathbb{C}^{M_U \times 1}. \tag{13}$$

### B. PROBLEM FORMULATION

Based on the DL and UL RF beamforming stages, we can write the total achieved Tx-to-Rx isolation $I_{\text{Tx-Rx}}$ as follows:

$$I_{\text{Tx-Rx}} = -10\log_{10}\left(\frac{1}{N}\sum\nolimits_n \left|\mathbf{f}_U^T(\hat{\theta}_U)\mathbf{H}_{SI}(:,:,n)\mathbf{f}_D(\hat{\theta}_D)\right|^2\right), \tag{14}$$

where $n = 1, 2, \ldots, N$ is the sample frequency point for a total of $N$ frequency points in a given bandwidth. If we steer the UL and DL beams to the desirable directions (i.e. $\hat{\theta}_U = \theta_U, \hat{\theta}_D = \theta_D$), then the DL and UL directivities are the maximum, which are given as follows:

$$|\Phi_D^T(\theta_D)\mathbf{f}_D(\hat{\theta}_D)|^2 = M_D, \quad |\mathbf{f}_U^T(\hat{\theta}_U)\Phi_U(\theta_U)|^2 = M_U. \tag{15}$$

For an FD massive MIMO system consisting of DL and UL RF beamformers $\mathbf{f}_D$ and $\mathbf{f}_U$, the total Tx-to-Rx isolation can be enhanced by the joint optimization of UL and DL beam steering angles $\hat{\theta}_U$, $\hat{\theta}_D$. We can formulate the optimization problem for Tx-to-Rx isolation as follows:

$$\begin{aligned} \min_{\{\hat{\theta}_D, \hat{\theta}_U\}} \quad & \frac{1}{N}\sum\nolimits_n \left|\mathbf{f}_U^T(\hat{\theta}_U)\mathbf{H}_{SI}(:,:,n)\mathbf{f}_D(\hat{\theta}_D)\right|^2 \\ \text{s.t.} \quad & C_1: \ |\hat{\theta}_U - \theta_U| \leq \epsilon, \\ & C_2: \ |\hat{\theta}_D - \theta_D| \leq \epsilon, \end{aligned} \tag{16}$$

where $C_1$ and $C_2$ refer to the beam angle perturbation constraints in desired UL and DL beam directions, respectively. In other words, the constraints limit the beam angle variation from the target beam steering directions $\theta_U$ and $\theta_D$ to value $\epsilon$. The optimization problem defined in (16) is non-convex and intractable due to the non-linearity constraints.

### C. RF BEAMFORMER DESIGN

The Tx-to-Rx isolation can be enhanced by designing the UL and DL RF beamforming stages $\mathbf{f}_U$ and $\mathbf{f}_D$ in an FD massive MIMO system. In the following, we discuss two different design schemes for RF beamformers.

#### 1) MAX-DIRECTIVITY-BASED RF BEAMFORMER DESIGN

In this scheme, our objective is to enhance the Tx-to-Rx FD isolation by steering the beams at the UL and DL user locations (i.e., $\theta_D$ and $\theta_U$). Particularly, the beamforming steering weights focus on maximizing the power pattern peaks pointing toward the desired steering angle. Using the measured SI channel, which consists of LoS path

[1]The beamforming-based isolation solutions presented in this work can be applied to multiple UL and DL users, which is left as our future work.

components, we can write the effective reduced-size SI channel matrix seen from the BB-stage as follows:

$$\mathcal{H}_{SI}(:,:,n) = \mathbf{f}_U^T \mathbf{H}_{SI}(:,:,n)\mathbf{f}_D. \tag{17}$$

*Lemma 1: For an FD massive MIMO system with Tx and Rx antenna arrays, the mutual coupling ($S_{Beam}(\theta_D, \theta_U)$) between the Tx and Rx antenna arrays can be minimized by designing the DL RF beamformer $\mathbf{F}_D$ with steering coefficients $w_D$ and UL RF beamformer $\mathbf{F}_U$ with steering coefficients $w_U$ such that the following holds*:

$$S_{Beam}(\theta_D, \theta_U) \approx \mathbf{w}_U^T \mathbf{H}_{SI} \mathbf{w}_D \approx \mathbf{0}. \tag{18}$$

*Proof:* See Appendix. ■

By steering the beams at exact user locations, we can generate $M_D(M_U)$ DL (UL) beams with maximum directivity. Here, the design of DL and UL RF stages, which yield the max-directivity beams, can be given as follows [42]:

$$\mathbf{f}_D(\theta_D) = \frac{1}{\sqrt{M_D}}[1, e^{j2\pi d\cos(\theta_D)}, \cdots, e^{j2\pi d(M_D-1)\cos(\theta_D)}]^T \tag{19}$$

$$\mathbf{f}_U(\theta_U) = \frac{1}{\sqrt{M_U}}[1, e^{-j2\pi d\cos(\theta_U)}, \cdots, e^{-j2\pi d(M_U-1)\cos(\theta_U)}]^T. \tag{20}$$

The design of $\mathbf{f}_D$ and $\mathbf{f}_U$ require $\log_2(M_D)$ and $\log_2(M_U)$ bit resolution PSs to realize the steering vectors with the DL/UL angle-pair and satisfies the constant modulus constraint.

### 2) BEAM ANGLE-PERTURBATION-BASED RF BEAMFORMER DESIGN

The maximum number of beams that can be steered at the exact user location is limited by the number of Tx and Rx antennas. Moreover, the max-directivity scheme can only provide high beam isolation at certain UL-DL $(\theta_U, \theta_D)$ angle-pairs. To overcome this limitation, a tradeoff between the beam gain and isolation level can result in an increased Tx-to-Rx isolation. In the proposed beam-perturbation-based RF beamformer design, both UL and DL RF stages are constructed by pointing the beams to $\hat{\theta}_D$ and $\hat{\theta}_U$ instead of the exact user locations $\theta_D$ and $\theta_U$. In other words, the Tx and Rx beams are allowed to vary in a range of $\theta_D \pm \Delta_D$ and $\theta_U \pm \Delta_U$ to search for the deep radiation nulls close to the UL and DL user location. Using the exhaustive search, the UL and DL beam-perturbed angles are found within 3dB-beamwidth around the desired UL and DL angles (i.e., $\theta_D$ and $\theta_U$). By tilting the beams from the exact user location can yield a better Tx-to-Rx isolation while satisfying the 3dB-beamwidth constraint in both UL and DL user directions.

The pseudo-code of the proposed beam-perturbation-based RF beamformer design is outlined in Algorithm 1. The algorithm can be summarized in the following steps: 1) Define the search space to specify the range of possible perturbations, $\Delta_{\max}$, which is determined based on the maximum 3-dB beamwidth that satisfies the constraint. For instance, the average 3dB-beamwidth of a $1 \times 4$ array (i.e., $M_D = M_U = 4$) is around 30°. Then, $\Delta_D$ and $\Delta_U$ are chosen to be half of this value, i.e. 15°, which means a maximum half beam power decrease is allowed in trade of isolation level; 2) discretize the search space by dividing it into discrete steps or intervals. For example, the search space can be formulated using increments of 1° or smaller, however, the smaller the resolution, the higher the computational complexity and the iterations in the measurements; 3) calculating or measuring the objective function (16) for each UL-DL perturbed-angle pair $(\hat{\theta}_U, \hat{\theta}_D)$ for min SI; 4) performing exhaustive search by iterating through all possible values of $(\Delta_D, \Delta_U)$ within the defined search space. For each $(\Delta_D, \Delta_U)$, calculate the corresponding $\hat{\theta}_D$ and $\hat{\theta}_U$ based on the perturbation equations and evaluate the objective function for each combination of $\hat{\theta}_D$ and $\hat{\theta}_U$; and 5) choose the optimal perturbed angles, which yields the minimum value of the objective function (16). These angles provide the best trade-off between beam gain and isolation while satisfying the 3dB-beamwidth constraint. Then, the UL and DL RF beamforming stages are constructed using (13) and (12), respectively.

**Algorithm 1** Proposed Beam-Perturbation-Based RF Beamformer Design Algorithm

**Input**: $(\theta_D, \theta_U)$, $M_D$, $M_U$, $\Delta_{\max}$ (based on 3-dB beamwidth constraint) $\mathbf{H}_{SI}$.
**Output**:$\hat{\theta}_D, \hat{\theta}_U, \mathbf{f}_D(\hat{\theta}_D), \mathbf{f}_U(\hat{\theta}_U)$
Discretize the search space: Divide the range into discrete steps of 1°
Initialize $\hat{\theta}_D \leftarrow 0, \hat{\theta}_U \leftarrow 0$.
**for** *each* $\Delta_D$ *in search space* **do**
  **for** *each* $\Delta_U$ *in search space* **do**
    Calculate $\hat{\theta}_D$ and $\hat{\theta}_U$ using $(\Delta_D, \Delta_U)$
    Formulate UL and DL RF beamformers $\mathbf{f}_U$ and $\mathbf{f}_D$ using (13), (12), respectively.
    Evaluate (16) using $\mathbf{f}_U$, $\mathbf{f}_D$, and $\mathbf{H}_{SI}$.
  **end**
**end**
Find $(\Delta_{D,opt}, \Delta_{U,opt})$ minimizing the objective function $|\mathbf{w}_U^T \mathbf{H}_{SI}(\theta_D \pm \Delta, \theta_U \pm \Delta)\mathbf{w}_D|$.
Find $\hat{\theta}_D = \theta_D + \Delta_{D,opt}, \hat{\theta}_U = \theta_U + \Delta_{U,opt}$.
Construct $\mathbf{f}_D(\hat{\theta}_D)$ and $\mathbf{f}_U(\hat{\theta}_U)$ using (13), (12).

## V. ILLUSTRATIVE MEASURED RESULTS

The $8 \times 8$Tx/$8 \times 8$Rx cross-polarized rectangular antenna array prototype is used for the radiation patterns and self-interference channel measurements, and the placement in the anechoic chamber is shown in Fig.14. The anechoic chamber is equipped with C-RAM SFC-48 absorber to minimize reflections and external interference and has a dimension of 6.1m $\times$ 2.4m $\times$ 2.4m (length $\times$ width $\times$ height). The vector network analyzer (VNA) with an output power of 10 dBm is used for SI measurements. In the

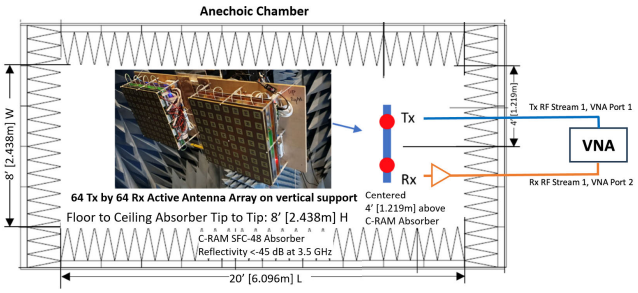


**FIGURE 14.** FD massive MIMO prototype setup in the anechoic chamber.

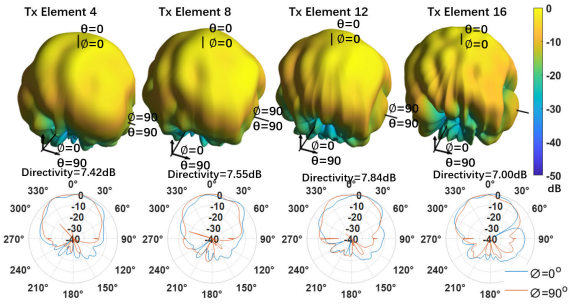


**FIGURE 15.** Measured 3D/2D-cut radiation patterns of Tx elements 4, 8, 12, 16.

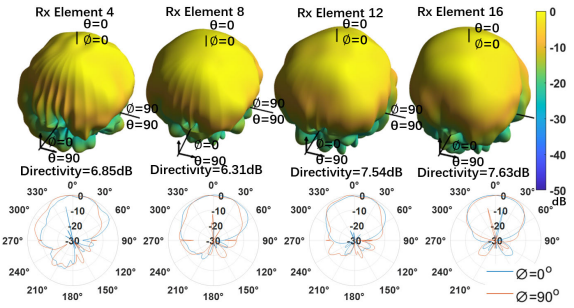


**FIGURE 16.** Measured 3D/2D-cut radiation patterns of Rx elements 4, 8, 12, 16.

Tx-to-Rx element MC measurements, to minimize the number of connections, 1-to-16 RF switches are used to control the on/off status of the Tx/Rx elements. In each measurement, only a single Tx element is excited. The resulting parameters are transmitted to the PC via Ethernet cable for SI channel characterization and then 64 × 64 two-port S-parameter files are combined to achieve the SI data of the 64 Tx elements to 64 Rx elements.

Two sample sub-arrays,[2] Tx 1 × 4 and Rx 1 × 4 are used for the beamforming and beamforming isolation measurements. For the Tx 1 × 4, the pre-calculated steering weight vector will be used to control 4 phase shifters and 4 attenuators. Within the feeding network, each antenna element is connected to a digitally controlled attenuator with seven bits, offering a 32 dB range with a 0.25 dB step size. This is followed by

[2]We have performed measurements with various $N \times M$ sub-arrays. For illustration, we only present the results of 1 × 4 sub-arrays in this section.

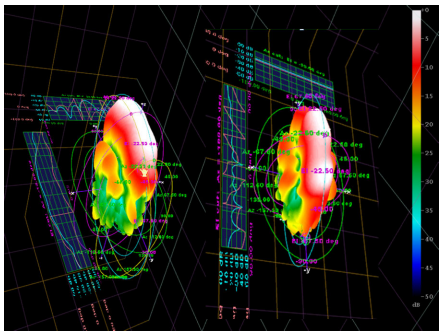

**FIGURE 17.** Measured Tx(left)/Rx(right) 1 × 4 sub-array beams at 3.5 GHz.

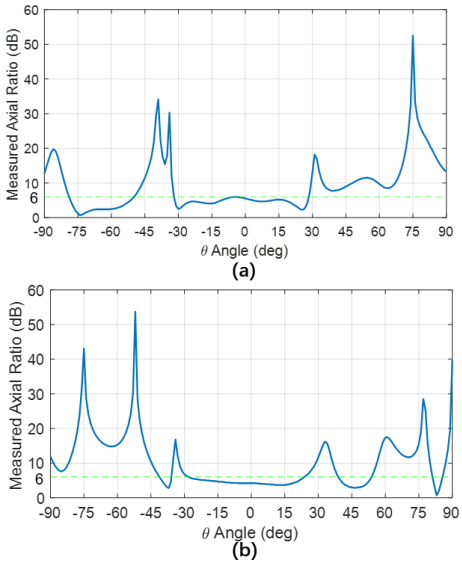


**FIGURE 18.** Measured beam axial ratio at cut at $\phi$=0° (a) Tx 1 × 4 sub-array beam; (b) Rx 1 × 4 sub-array beam.

a digitally controlled phase shifter with six bits, providing a 360° coverage with a step size of 5.625° enabling precise control over the phase of the signals. Before the signal is fed to the antenna, the final stage RF amplifiers are connected directly to each antenna element to maximize transmitted power and compensate for the insertion loss of the system.

On the receiving side, the sub-array will be connected directly to low-noise amplifiers (LNA) and then to 4 power attenuators and 4 phase shifters. Due to the reason that the MC signals can be very weak after the stages of antenna isolation and beam level MC suppression, the LNA is used to improve the measurement sensitivity by increasing the signal-to-noise ratio (SNR). Then the signals from the four paths will be combined from a 4-to-1 power combiner and sent to the Spectrum Analyzer or the VNA. Furthermore, the components of our design are interconnected using short coaxial cables and compact JSC connectors, all of which are arranged behind the antenna arrays for efficiency and convenience. Control of the feeding network is facilitated by a custom Serial Peripheral Interface (SPI) module housed within a Raspberry Pi 4.

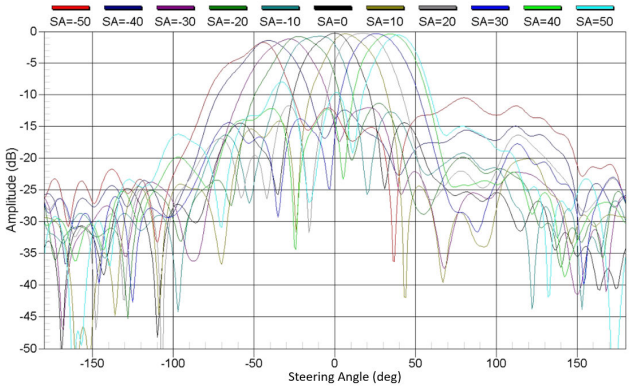


**FIGURE 19.** Measured Tx 1 × 4 sub-array beam steering 2D cut for steering angle from −50° to +50°.

**TABLE 3.** Tx 1 × 4 sub-array beam steering measurement results.

| Steering angle (deg) | Achieved Angle (deg) | Directivity (dB) | 3dB BW(deg) | 10dB BW (deg) | SLL (dB) |
|---|---|---|---|---|---|
| 50 | 41.0 | 11.3 | 23.8 | 43.0 | -9.0 |
| 45 | 39.0 | 11.2 | 25.8 | 44.5 | -10.0 |
| 40 | 38.0 | 11.0 | 28.0 | 46.5 | -11.9 |
| 35 | 31.7 | 10.8 | 28.8 | 48.1 | -12.9 |
| 30 | 26.6 | 10.8 | 29.0 | 49.1 | -13.4 |
| 25 | 22.7 | 10.9 | 29.0 | 48.8 | -11.6 |
| 20 | 14.9 | 10.9 | 29.3 | 47.2 | -11.4 |
| 15 | 10.1 | 11.3 | 28.7 | 47.4 | -11.8 |
| 10 | 7.0 | 11.5 | 26.6 | 48.3 | -13.8 |
| 5 | 3.5 | 11.5 | 24.5 | 48.0 | -16.4 |
| 0 | -1.2 | 11.3 | 27.3 | 47.9 | -14.1 |
| -5 | -7.5 | 11.2 | 29.0 | 48.0 | -12.4 |
| -10 | -12.4 | 11.1 | 30.8 | 48.7 | -11.9 |
| -15 | -16.8 | 11.1 | 31.1 | 50.8 | -10.5 |
| -20 | -21.0 | 11.0 | 30.1 | 54.3 | -10.6 |
| -25 | -27.2 | 10.7 | 32.9 | 58.9 | -10.9 |
| -30 | -31.0 | 11.0 | 30.8 | 57.1 | -10.8 |
| -35 | -35.3 | 10.9 | 33.0 | 60.4 | -10.7 |
| -40 | -40.6 | 10.7 | 30.0 | 61.0 | -11.0 |
| -45 | -49.0 | 10.8 | 26.8 | 59.8 | -11.2 |
| -50 | -51.2 | 10.8 | 29.1 | 57.5 | -10.3 |

### A. MEASURED ELEMENT PATTERNS IN THE SAMPLE SUB-ARRAYS

The measured radiation patterns of the four Tx elements and four Rx elements of the sample 1 × 4 sub-arrays are shown in Fig. 15 and Fig. 16. It can be observed that both the Tx and Rx antennas exhibit radiation pattern distortions and a tendency to lean towards the array center for the edge elements (Tx element 13 and Rx element 4). The average directivity is 7.5 dB for the Tx elements and 7.1 dB for the Rx elements. For the Tx sub-array, the edge element has a directivity of 0.4 dB lower than the directivity of the center element, and for the Rx sub-array, this difference is 0.8 dB.

### B. TX 1 × 4/RX 1 × 4 SUB-ARRAY BEAM MEASUREMENTS

#### 1) SUB-ARRAY 3D BEAM PATTERN

The measured 3D beams of the Tx 1 × 4 and the Rx 1 × 4 sub-arrays with uniform feeding power and zero phase shift in the anechoic chamber are shown in Fig. 17. Both sub-arrays get a plate-shaped beam, with two sidelobes on the two sides of the main beam. The directivity of the Tx 1 × 4 sub-array is 11.3 dB, and the directivity of the Rx 1 × 4 sub-array is 11.9 dB. The Tx and Rx 1 × 4 sub-array realized gain is 9.1 dB and 9.4 dB, respectively, which indicates a radiation efficiency of 61.0% and 55.6%. The Tx and Rx sub-arrays have 3dB-beamwidths of 27.3° and 28.7° in the $\theta$ plate, respectively. Both the Tx and the Rx sub-arrays have normalized sidelobe levels of -14.1 dB and first null beamwidths of 66°.

**TABLE 4.** Rx 1 × 4 sub-array beam steering measurement results.

| Steering angle (deg) | Achieved Angle (deg) | Directivity (dB) | 3dB BW(deg) | 10dB BW (deg) | SLL (dB) |
|---|---|---|---|---|---|
| 50 | 46.4 | 10.5 | 32.7 | 51.4 | -10.1 |
| 45 | 40.9 | 10.8 | 32.1 | 51.9 | -10.8 |
| 40 | 35.9 | 11.3 | 29.4 | 54.6 | -9.7 |
| 35 | 33.8 | 11.4 | 30.1 | 55.0 | -13.6 |
| 30 | 31.7 | 11.5 | 29.8 | 52.2 | -14.9 |
| 25 | 18.2 | 11.6 | 28.6 | 48.6 | -11.8 |
| 20 | 17.4 | 11.8 | 28.4 | 47.5 | -13.8 |
| 15 | 14.0 | 12.1 | 27.4 | 47.9 | -13.8 |
| 10 | 10.1 | 12.1 | 28.2 | 47.8 | -13.8 |
| 5 | 4.7 | 12.0 | 30.7 | 50.6 | -14.4 |
| 0 | 0.0 | 11.9 | 28.7 | 48.8 | -14.1 |
| -5 | -5.2 | 11.8 | 27.1 | 47.2 | -15.0 |
| -10 | -6.2 | 11.5 | 26.5 | 46.8 | -12.1 |
| -15 | -15.6 | 11.3 | 26.8 | 46.9 | -11.7 |
| -20 | -16.8 | 11.1 | 26.8 | 49.6 | -11.5 |
| -25 | -23.0 | 10.9 | 26.0 | 45.9 | -10.6 |
| -30 | -25.1 | 10.6 | 24.8 | 46.4 | -8.1 |
| -35 | -29.6 | 10.1 | 23.3 | 43.4 | -10.9 |
| -40 | -30.4 | 9.8 | 23.0 | 115.7 | -8.1 |
| -45 | -31.4 | 9.4 | 23.0 | 116.7 | -4.6 |
| -50 | -34.9 | 8.6 | 23.5 | 47.6 | -8.9 |

#### 2) SUB-ARRAY BEAM AXIAL RATIO

The AR measurement results of the proposed Tx 1 × 4 and Rx 1 × 4 sub-arrays at steering angle $\theta = 0°$ are presented in Fig. 18. It can be seen that the Tx and Rx sub-arrays attain a minimum AR of 2.3 dB and 2.8 dB, respectively, in the main lobe range. The AR is consistently lower than 6 dB, in the $\theta$ angle range of −32° to 28° for the Tx sub-array and in the range of −28° to 23° for the Rx sub-array, which is approximately equal to the main lobe beamwidth. A considerable fluctuation in the AR can be detected beyond this range, potentially leading to a cross-polarization ratio loss in the beam isolation performance.

### C. TX 1 × 4/RX 1 × 4 SUB-ARRAY BEAM STEERING MEASUREMENTS

#### 1) TX 1 × 4 SUB-ARRAY BEAMFORMING

The 2D cuts of the measured Tx 1 × 4 sub-array beamforming results for steering angle from −50° to +50° are shown in Fig. 19 and Table 3. The steering weights used in the simulations have a uniform magnitude, and phase shift values are changed based on the steering angle, as shown in (13) and (12), respectively. The average directivity is 11.0 dB. The directivity variation in the steering range is 0.9 dB. Within the steering range, the average 3dB-beamwidth and 10dB-beamwidth are 28.8° and 51.2°, respectively. The sidelobe level (SLL) is consistently lower than −9.0 dB

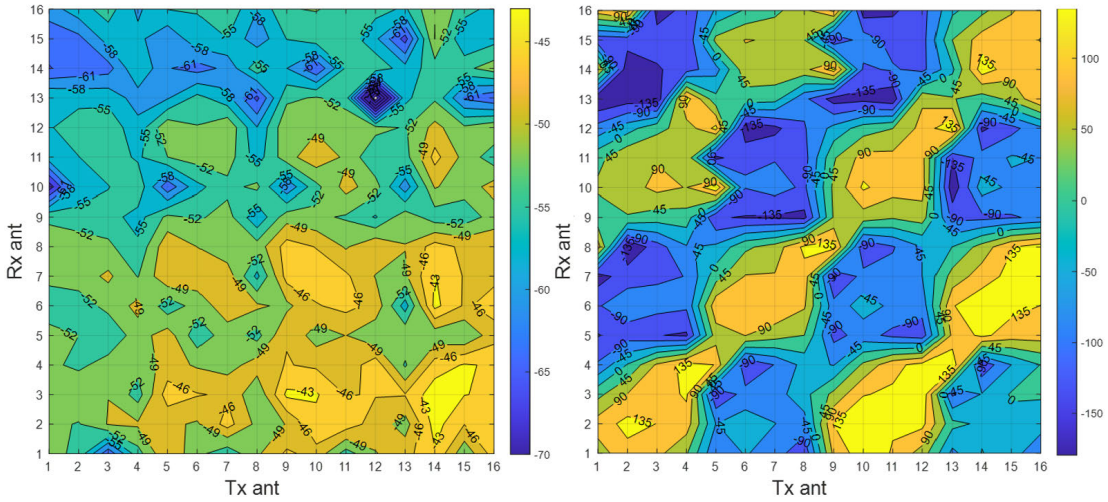


**FIGURE 20.** Measured MC between Tx and Rx elements: magnitude (dB) (left) and phase (degree) (right) at 3.5 GHz.

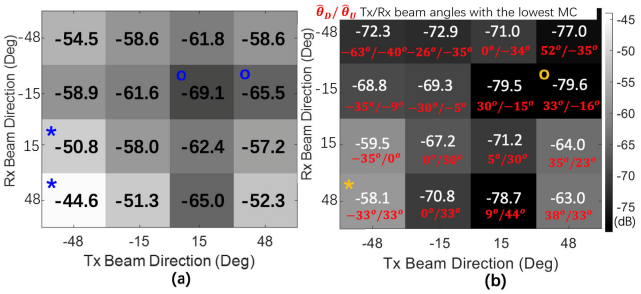


**FIGURE 21.** Measured Tx-to-Rx MC level of sub-arrays with (a) max-directivity-based beamformer; (b) angle-perturbation-based beamformer.

across the steering range and lower than −10.3 dB within the steering range from −50° to +40°. With the uniform magnitude steering vectors, the difference between the achieved and target beam directions is less than 5° within the steering range of −50° to 40° for the Tx 1 × 4 sub-array.

Compared with the simulation results of the Right 1 × 4 sub-array, which has a similar relative location in the array, the Tx 1 × 4 sub-array exhibits a similar trend in beam peak angle tilt, directivity, beamwidth, and sidelobe level change. When the beam is steering away from the array center, the sub-array with an asymmetric location on the array tends to have narrower 3dB- and 10dB-beamwidths and an average beam tilted of −3.8°, which is on average −1.1° more tilted than the simulation results. The average directivity and sidelobe level difference between the simulated and the measured values are 0.2 dB and 1.0 dB, respectively.

#### 2) RX 1 × 4 SUB-ARRAY BEAMFORMING

The measured Rx 1 × 4 sub-array beamforming results with steering angles from −50° to +50° are shown in Table 4, respectively. Within the steering range, the average directivity is 11.1 dB. The average 3dB- and 10dB- beamwidths are 27.5° and 55.4°, respectively. When the beam is steering away from the array center, i.e., $\theta < 0°$, the Rx sub-array tends to have a relatively narrower 3dB- and 10dB-beamwidth, and the sidelobe level increases fast. The sidelobe level is lower than −8.1 dB at all steering angles except at the steering angle of −45°. The sidelobe level is lower than −9.7 dB within the steering range from −25° to +50°.

### D. TX/RX ELEMENT MUTUAL COUPLING MEASUREMENT

As labelled in Fig. 2, Tx/Rx element MC measurement is done using the 16 elements on the right-top quarter area of the Tx array and the 16 elements on the left-top quarter of the Rx array, which are separated by 20 cm. The data is collected for a frequency range from 3.35 GHz to 3.6 GHz. The measured MC magnitude (in dB) and the phase plots at sample 3.5 GHz are shown in Fig. 20.

Across the 256 MC combinations, an average of −49.2 dB is achieved, which shows an average 0.8 dB lower MC compared with the simulation results of elements on two 4 × 4 arrays with the same relative position. Examining the magnitude plot, we observe that the lower right region, representing the MC between Tx elements 9 to 16 and Rx elements 1 to 8, exhibits a relatively higher MC level with an average of −45.7 dB. Conversely, the upper left region, corresponding to the MC between Tx elements 1 to 8 and Rx elements 9 to 16, demonstrates a lower MC magnitude with an average of −54.7 dB, which is about 9.0 dB lower (better) than the right bottom region. Distance remains an influential factor in the MC level, and the increased number of EBG patches between the Tx and Rx elements also contributes to the observed isolation improvement. A periodic pattern of MC phase change with the distance $\lambda_0/2$ increase can be observed in the phase plot. A potential isolation improvement can be achieved at the beam level when antenna sub-arrays are used.

### E. RF BEAMFORMING-BASED MEASUREMENT RESULTS

The beam isolation is measured with the sample Tx $1 \times 4$ and Rx $1 \times 4$ sub-arrays, as labelled in Fig. 2. A 20 MHz band (3.49 GHz to 3.51 GHz) modulated signal is used in the beam MC measurements. Since the first null beamwidth of both Tx and Rx $1 \times 4$ sub-arrays is around 66°, i.e., 33° away from the beam peak direction, four steering angles with 30° to 33° separation are used in the measurements, which are $-48°, -15°, 15°$, and 48°. Therefore, a total of 16 Tx and Rx beam angle combinations are measured. The Tx-to-Rx beam MC values with the two beamforming schemes as discussed in Section IV are measured in the anechoic chamber. Moreover, the far-field beam patterns of both Tx and Rx $1 \times 4$ sub-arrays at the corresponding steering angles are presented.

#### 1) MAX-DIRECTIVITY-BASED RF-BEAMFORMER PERFORMANCE

##### a: MEASURED MUTUAL COUPLING RESULTS

The measured MC levels are shown in Fig. 21(a). Across the 16 beamforming combinations, an average MC level is −53.6 dB and a minimum MC level of −69.1 dB can be achieved. Compared with the measured MC between Tx and Rx elements, the beam level isolation is improved by 4.4 dB on average. Among the test cases, 11 Tx-Rx angle pairs (69%) achieve an MC level lower (better) than −57 dB. Steering Tx and Rx beams in the direction across each other leads to an average 13.3 dB lower MC compared with the case when two beams are steering away from each other. Additionally, it can be seen that an average MC of -59.6 dB is attained when the Rx beam steers at the Tx beam null location, i.e., 33° away from the Tx peak direction, which shows an average 10.4 dB isolation improvement compared with the element MC value and on average 7.6 dB lower in comparison to the beam MC level at other steering angle combinations.

##### b: FAR-FIELD BEAM PATTERN INFLUENCE ON THE BEAM MC

The measured four sample pairs of Tx/Rx far-field beam patterns are plotted. The Tx/Rx beams with the two highest MC levels (as highlighted by the blue star in Fig. 21(a)) are shown in Fig. 22(a) and (b). Meanwhile, the Tx/Rx beams with the two best MC values (as highlighted by the blue circle in Fig. 21(a)) are shown in Fig. 22(c) and (d). The Tx beam is plotted in a cross-polarization (X-pol) state, i.e., LCHP status, to showcase the far-field radiation intensity of the Tx beam in the co-polarization (Co-pol) state with the Rx beam.

Remarkably, a strong correlation between the Tx/Rx far-field patterns and the beam MC can be observed. The measured beam patterns illustrate that, on average, the two highest MC beam pairs are 20.3 dB higher than the two lowest beam MC. Similarly, when comparing the Tx far-field radiation intensity within the 3dB-beamwidth range of the Rx beam, the radiation intensity of the two highest beam pairs is, on average, 9.5 dB higher. Empirical evidence demonstrates that the far-field component plays an important role as a contributor to the total beam MC.

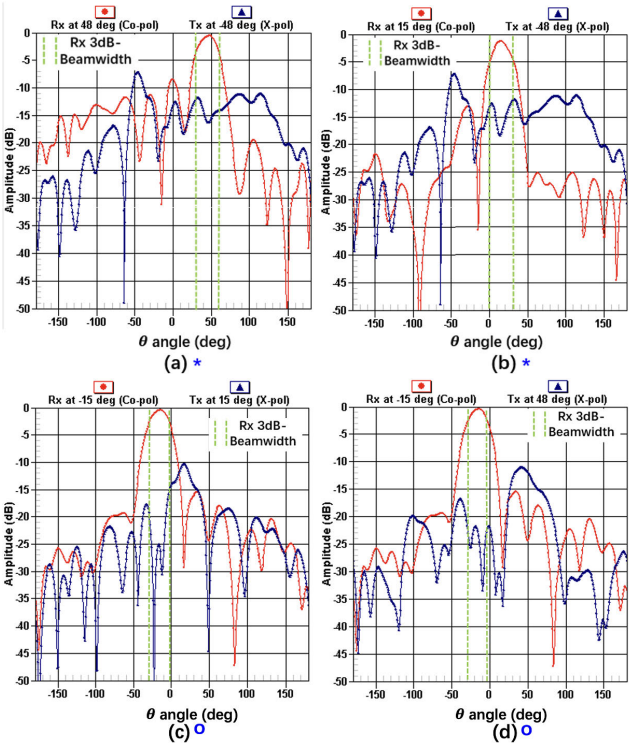


**FIGURE 22.** Measured Tx/Rx $1 \times 4$ sub-array beam radiation pattern 2D cuts Scheme 1 at 3.5 GHz. The Tx/Rx beam combinations with the highest MC (a) and (b). The Tx/Rx beam combinations with the lowest MC (c) and (d).

When the Tx beams have negative steering angles, the Tx radiation intensity in the Rx main lobe direction is relatively stronger than when steering it in the positive angles. For example, when the Tx beam steering is at −48°, a relatively high Tx radiation power with shallow radiation nulls (worse than −18 dB) in the Rx main lobe direction can be observed. When the Tx beam is steering at 15° and 48°, the Tx beam has deeper null (lower than −25 dB) in the Rx main lobe range.

Furthermore, it can be seen that there is more than a 10 dB discrepancy between the average beam isolation level and the corresponding far-field radiation intensity difference. This difference can be caused mostly by the near-field leakage wave, which indicates that the near-field coupling is still an important source of the total MC.

#### 2) ANGLE-PERTURBATION-BASED BEAMFORMER PERFORMANCE

##### a: MEASURED MUTUAL COUPLING RESULTS

This section investigates beam isolation improvement with Tx/Rx angle optimization when the beam direction varies within a tolerance range. The measured lowest MC results within the half 3dB-beamwidth constraint, along with the corresponding beam steering angles, are shown in Fig. 21(b). An average MC level of −65.6 dB was observed throughout the 16 beamforming combinations, which is 16.4 dB lower (better) on average than the average Tx-to-Rx element MC values. The MC level is lower than −58.1 dB in all 16 beam

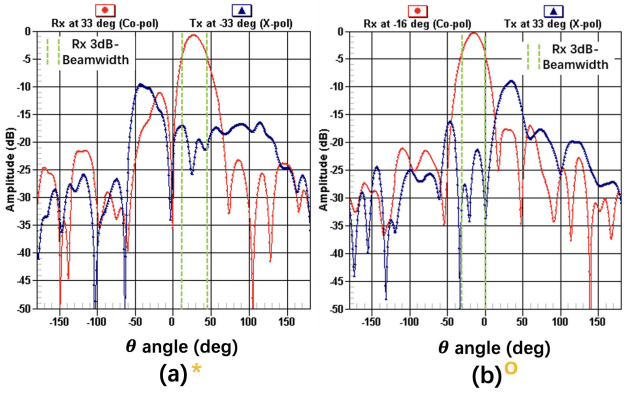


**FIGURE 23.** Measured Tx/Rx 1 × 4 sub-array beam radiation pattern 2D cuts Scheme 2 at 3.5 GHz. The Tx/Rx beam combinations with the highest MC (a). The Tx/Rx beam combinations with the lowest MC (b).

angle pairs, which indicates a 13.5 dB isolation improvement compared with the highest MC in scheme 1. When the Tx and Rx beams are steering across each other (right top quarter of the Fig. 21(b)), an average −75.2 dB MC is attained, which is 13.8 dB lower than the average MC when steering two beams away from each other (left bottom quarter of the Fig. 21(b)).

An average MC reduction of 12.0 dB is achieved when compared to scheme 1 results. The largest isolation improvement is 19.5 dB at −15° Tx beam and 48° Rx beam. Additionally, it can be observed that the best isolation typically occurs at 15° away from the intended direction, which has approximately 3 dB lower power than the beam peak. As a result, there is a tradeoff between a maximum loss of 3 dB of desired signal strength and an average improvement of 12.0 dB isolation level in the beamforming.

#### *b: FAR-FIELD BEAM PATTERN INFLUENCE ON THE BEAM MC*

The two samples (the highest and the lowest beam MC cases) of measured far-field beam pattern 2D cuts after beam steering angle perturbation are plotted, as shown in Fig. 23. When comparing Fig. 22(a) and Fig. 23(a), which is the beam pair with the highest MC in the two schemes, the Tx radiation power in the Rx 3dB-beamwidth range direction is lowered by 6.2 dB on average, which is potentially one of the main contributors to the 13.5 dB beam isolation improvement. Comparing the Tx/Rx beam patterns of the lowest MC pair (Tx steering angle at 33° and Rx steering angle at −16°), the Tx beam has very deep nulls (lower than −30 dB) and an average −26.5 dB normalized power level in the Rx beam 3dB-beamwidth angle range. The observation is consistent with the previous section.

The findings also suggest that methods such as directing the Rx beam towards the radiation nulling range of the Tx beam or creating arbitrary deep nulls via adaptive beamforming techniques in the beamformer design can effectively enhance the Tx-to-Rx beam isolation in FD communications.

## VI. CONCLUSION

In this paper, a prototype pair of 8 × 8Tx/8 × 8Rx antenna arrays for FD massive MIMO with dual-layer EBG slotted circularly polarized patch antenna elements and orthogonal Tx-Rx polarization is developed and fabricated. The size of the radiating patch is reduced by 65% area. An average MC between Tx and Rx antenna elements of −49.2 dB can be achieved. Theoretical estimation of the linear array directivity and beamwidth change with the number of elements change are investigated and compared with different simulation scenarios. It is shown that the element pattern has less effect on the array directivity and beamwidth with the increased number of elements. Sample Tx 1 × 4 and Rx 1×4 sub-arrays are used as samples to study the beamforming and beamforming isolation performance. Within a steering range from −50° to 50°, a directivity over 10.7 dB, a 3dB-beamwidth less than 33.0°, and a normalized sidelobe level lower than −9.0 dB are achieved. Two beamforming isolation improvement schemes are proposed and studied via direct experimental measurements. When a 3dB-beamwidth steering angle variation is allowed, the average beam MC level is lowered to -65.5 dB, which is 16.4 dB lower than the Tx-to-Rx element MC. A best beam isolation level of 79.6 dB can be achieved. The experiments also prove that relatively high beam isolation can be achieved by steering the Rx beams in the Tx beam far-field radiation null directions.

## APPENDIX
## PROOF OF LEMMA 1

Let $\mathbf{w}_U$ and $\mathbf{w}_D$ be the column vectors of steering coefficients for the UL ($\mathbf{f}_U$) and DL ($\mathbf{f}_D$) RF beamformers, respectively. Then we can write the effective SI ($\mathbf{w}_U^T \mathbf{H}_{SI} \mathbf{w}_D$) as follows:

$$\mathbf{w}_U^T \mathbf{H}_{SI} \mathbf{w}_D = \sum_{j=1}^{M_U} \sum_{i=1}^{M_D} w_{U,j}^* h_{ji,SI} w_{D,i}, \tag{21}$$

where $w_{U,j}$ is the complex conjugate of the steering coefficient for the $j^{th}$ Rx element, $w_{D,i}$ is the steering coefficient for the $i^{th}$ Tx element, and $h_{ji,SI}$ represents the SI channel coefficient between the $j^{th}$ Rx element and $i^{th}$ Tx element. The mutual coupling between the Tx and Rx antenna arrays is given as follows:

$$S_{Beam}(\theta_D, \theta_U) = \sum_j \sum_i w_{i,\theta_D}^* w_{j,\theta_U}^* S_{ji}, \tag{22}$$

where $w_{i,\theta_D}^*$ represents the complex conjugate of the steering coefficient for the $i^{th}$ Tx element at the beam steering angle $\theta_D$, $w_{j,\theta_U}^*$ represents the complex conjugate of the steering coefficient for the $j^{th}$ Rx element at the beam steering angle $\theta_U$, and $S_{ji}$ is the measured MC in complex value between the $i^{th}$ Tx element and $j^{th}$ Rx element. Substituting the expression for the SI term into the equation for mutual coupling, we can

write as:

$$S_{Beam}(\theta_D,\theta_U)=\sum_j\sum_i w^*_{i,\theta_D}w^*_{j,\theta_U}\sum_{j=1}^{M_U}\sum_{i=1}^{M_D} w^*_{U,j}h_{ji,SI}w_{D,i}. \tag{23}$$

*Remark 1:* The use of large array structures at BS for an FD massive MIMO system satisfies the following points: 1) the indices $i$ and $j$ can span a significant range, including elements that are physically distant from each other; and 2) the mutual coupling, $S_{Beam}(\theta_D,\theta_U)$, is a sum over all possible combinations of Tx and Rx elements. Many of these combinations involve elements that are physically distant and thus have small mutual coupling values. Due to the averaging effect, the mutual coupling term tends to be dominated by combinations of elements that are physically close and have significant mutual coupling values. Elements that are physically distant contribute less to the sum. As a result of the averaging effect and the dominance of physically close elements in the sum, we can approximate the mutual coupling as:

$$S_{Beam}(\theta_D,\theta_U)\approx\sum_{j=1}^{M_U}\sum_{i=1}^{M_D} w^*_{U,j}h_{ji,SI}w_{D,i}. \tag{24}$$

This approximation suggests that the mutual coupling between the Tx and Rx antenna arrays can be effectively minimized by designing the DL RF beamformer $\mathbf{F}_D$ with steering coefficients $w_D$ and UL RF beamformer $\mathbf{F}_U$ with steering coefficients $w_U$ such that the SI term $\mathbf{w}_U^T\mathbf{H}_{SI}\mathbf{w}_D$ approaches zero. Now, let us investigate the condition under which the mutual coupling, $S_{Beam}(\theta_D,\theta_U)$, can be minimized. To achieve this, we aim to minimize the SI term $\mathbf{w}_U^T\mathbf{H}_{SI}\mathbf{w}_D$. Our design objective is to find suitable steering coefficients $\mathbf{w}_U$ and $\mathbf{w}_D$ such that $\mathbf{w}_U^T\mathbf{H}_{SI}\mathbf{w}_D\approx\mathbf{0}$.

*Remark 2:* In massive MIMO systems employing large array structures, several key observations can be made:

- The SI channel coefficients, represented by $\mathbf{H}_{SI}$, often exhibit non-negligible magnitudes. This is because the Tx and Rx antennas within the same device are typically in close proximity, resulting in strong coupling.
- The steering coefficients, $w_U$ and $w_D$, determine the spatial focusing and alignment of the RF beams. Therefore, by carefully designing these coefficients, we can control the phases and amplitudes of the RF beams.

The effective SI can be given as:

$$\mathbf{w}_U^T\mathbf{H}_{SI}\mathbf{w}_D = \frac{1}{\sqrt{M_DM_U}}\sum_{m_u=1}^{M_U}\sum_{m_d=1}^{M_D}h_{m_u,m_d}e^{-j2\pi d(m_u\cos(\theta_U)-m_d\cos(\theta_D))}, \tag{25}$$

where $h_{m_u,m_d}$ is the $(m_u,m_d)^{th}$ element of $\mathbf{H}_{SI}$. By leveraging the properties of sinusoidal functions, the boundedness of $\cos(\theta_U)$ and $\cos(\theta_D)$, and the fact that $M_U$ and $M_D$ are sufficiently large, we can show that:

$$\begin{aligned}|m_u\cos(\theta_U)-m_d\cos(\theta_D)| &\le m_u|\cos(\theta_U)|+m_d|\cos(\theta_D)|\\ &\le m_u+m_d\le M_U+M_D-2.\end{aligned} \tag{26}$$

This result indicates that the phase term in $\mathbf{w}_U^T\mathbf{H}_{SI}\mathbf{w}_D$ is bounded. By applying the triangle inequality and analyzing the magnitude of $\mathbf{w}_U^T\mathbf{H}_{SI}\mathbf{w}_D$, we have:

$$|\mathbf{w}_U^T\mathbf{H}_{SI}\mathbf{w}_D|\le \frac{1}{\sqrt{M_DM_U}}(M_U+M_D-2)\max_{m_u,m_d}|h_{m_u,m_d}|. \tag{27}$$

Based on our assumptions that the path loss is significant and the SI channel is strong, we infer that the maximum absolute value of the SI channel coefficients $\max_{m_u,m_d}|h_{m_u,m_d}|$ is very small. As a consequence of the small maximum SI channel coefficient and the large dimensions of $M_U$ and $M_D$, we approximate the expression as:

$$S_{Beam}(\theta_D,\theta_U)\approx|\mathbf{w}_U^T\mathbf{H}_{SI}\mathbf{w}_D|\approx\mathbf{0}. \tag{28}$$

This approximation holds when the SI channel is strong, the path loss is significant, and large array structures are employed. Thus, for a given UL-DL angle-pair $\theta_D,\theta_U$ in an FD massive MIMO, the approximation $S_{Beam}(\theta_D,\theta_U)\approx|\mathbf{w}_U^T\mathbf{H}_{SI}\mathbf{w}_D|\approx\mathbf{0}$ holds. This approximation indicates the effective suppression of SI interference, leading to the minimization of mutual coupling ($S_{Beam}(\theta_D,\theta_U)$).

## REFERENCES


[1] P. Xingdong, H. Wei, Y. Tianyang, and L. Linsheng, "Design and implementation of an active multibeam antenna system with 64 RF channels and 256 antenna elements for massive MIMO application in 5G wireless communications," *China Commun.*, vol. 11, no. 11, pp. 16–23, Nov. 2014.

[2] S. Malkowsky, J. Vieira, L. Liu, P. Harris, K. Nieman, N. Kundargi, I. C. Wong, F. Tufvesson, V. Öwall, and O. Edfors, "The world's first real-time testbed for massive MIMO: Design, implementation, and validation," *IEEE Access*, vol. 5, pp. 9073–9088, 2017.

[3] E. G. Larsson, O. Edfors, F. Tufvesson, and T. L. Marzetta, "Massive MIMO for next generation wireless systems," *IEEE Commun. Mag.*, vol. 52, no. 2, pp. 186–195, Feb. 2014.

[4] A. Sabharwal, P. Schniter, D. Guo, D. W. Bliss, S. Rangarajan, and R. Wichman, "In-band full-duplex wireless: Challenges and opportunities," *IEEE J. Sel. Areas Commun.*, vol. 32, no. 9, pp. 1637–1652, Sep. 2014.

[5] A. Shojaeifard, K.-K. Wong, M. Di Renzo, G. Zheng, K. A. Hamdi, and J. Tang, "Massive MIMO-enabled full-duplex cellular networks," *IEEE Trans. Commun.*, vol. 65, no. 11, pp. 4734–4750, Nov. 2017.

[6] F. Chen, H. H. Lee, R. Morawski, and T. Le-Ngoc, "RF/analog self-interference canceller for 2×2 MIMO full-duplex transceiver," in *Proc. IEEE Int. Conf. Commun. (ICC)*, Paris, France, May 2017, pp. 1–6.

[7] M. Chung, M. S. Sim, J. Kim, D. K. Kim, and C.-B. Chae, "Prototyping real-time full duplex radios," *IEEE Commun. Mag.*, vol. 53, no. 9, pp. 56–63, Sep. 2015.

[8] T. Riihonen, S. Werner, R. Wichman, and J. Hamalainen, "Outage probabilities in infrastructure-based single-frequency relay links," in *Proc. IEEE Wireless Commun. Netw. Conf.*, Apr. 2009, pp. 1–6.

[9] Y. Hua, P. Liang, Y. Ma, A. C. Cirik, and Q. Gao, "A method for broadband full-duplex MIMO radio," *IEEE Signal Process. Lett.*, vol. 19, no. 12, pp. 793–796, Dec. 2012.

[10] M. Duarte, A. Sabharwal, V. Aggarwal, R. Jana, K. K. Ramakrishnan, C. W. Rice, and N. K. Shankaranarayanan, "Design and characterization of a full-duplex multiantenna system for WiFi networks," *IEEE Trans. Veh. Technol.*, vol. 63, no. 3, pp. 1160–1177, Mar. 2014.

[11] W. T. Slingsby, "Antenna isolation measurements for on-frequency radio repeaters," in *Proc. 9th Int. Conf. Antennas Propag. (ICAP)*, 1995, pp. 239–243.
[12] B. Debaillie, D.-J. van den Broek, C. Lavín, B. van Liempd, E. A. M. Klumperink, C. Palacios, J. Craninckx, B. Nauta, and A. Pärssinen, "Analog/RF solutions enabling compact full-duplex radios," *IEEE J. Sel. Areas Commun.*, vol. 32, no. 9, pp. 1662–1673, Sep. 2014.
[13] H. Nawaz and I. Tekin, "Dual-polarized, differential fed microstrip patch antennas with very high interport isolation for full-duplex communication," *IEEE Trans. Antennas Propag.*, vol. 65, no. 12, pp. 7355–7360, Dec. 2017.
[14] S. Ghosh, T.-N. Tran, and T. Le-Ngoc, "Dual-layer EBG-based miniaturized multi-element antenna for MIMO systems," *IEEE Trans. Antennas Propag.*, vol. 62, no. 8, pp. 3985–3997, Aug. 2014.
[15] H. S. Farahani, M. Veysi, M. Kamyab, and A. Tadjalli, "Mutual coupling reduction in patch antenna arrays using a UC-EBG superstrate," *IEEE Antennas Wireless Propag. Lett.*, vol. 9, pp. 57–59, 2010.
[16] G. Zhai, Z. N. Chen, and X. Qing, "Enhanced isolation of a closely spaced four-element MIMO antenna system using metamaterial mushroom," *IEEE Trans. Antennas Propag.*, vol. 63, no. 8, pp. 3362–3370, Aug. 2015.
[17] A. Dadgarpour, B. Zarghooni, B. S. Virdee, T. A. Denidni, and A. A. Kishk, "Mutual coupling reduction in dielectric resonator antennas using metasurface shield for 60-GHz MIMO systems," *IEEE Antennas Wireless Propag. Lett.*, vol. 16, pp. 477–480, 2017.
[18] Y. Liu, P. Roblin, X. Quan, W. Pan, S. Shao, and Y. Tang, "A full-duplex transceiver with two-stage analog cancellations for multipath self-interference," *IEEE Trans. Microw. Theory Techn.*, vol. 65, no. 12, pp. 5263–5273, Dec. 2017.
[19] K. E. Kolodziej, J. G. McMichael, and B. T. Perry, "Multitap RF canceller for in-band full-duplex wireless communications," *IEEE Trans. Wireless Commun.*, vol. 15, no. 6, pp. 4321–4334, Jun. 2016.
[20] J. W. Kwak, M. S. Sim, I.-W. Kang, J. Park, K.-K. Wong, and C.-B. Chae, "Analog self-interference cancellation With practical RF components for full-duplex radios," *IEEE Trans. Wireless Commun.*, vol. 22, no. 7, pp. 4552–4564, Jul. 2023.
[21] E. Ahmed and A. M. Eltawil, "All-digital self-interference cancellation technique for full-duplex systems," *IEEE Trans. Wireless Commun.*, vol. 14, no. 7, pp. 3519–3532, Jul. 2015.
[22] S. Khaledian, F. Farzami, B. Smida, and D. Erricolo, "Inherent self-interference cancellation for in-band full-duplex single-antenna systems," *IEEE Trans. Microw. Theory Techn.*, vol. 66, no. 6, pp. 2842–2850, Jun. 2018.
[23] D. Lee and B.-W. Min, "1-TX and 2-RX in-band full-duplex radio front-end with 60 dB self-interference cancellation," in *IEEE MTT-S Int. Microw. Symp. Dig.*, May 2015, pp. 1–4.
[24] E. Everett, M. Duarte, C. Dick, and A. Sabharwal, "Empowering full-duplex wireless communication by exploiting directional diversity," in *Proc. 45th Asilomar Conf. Signals, Syst. Comput. (ASILOMAR)*, Nov. 2011, pp. 2002–2006.
[25] Z. Zhang, X. Chai, K. Long, A. V. Vasilakos, and L. Hanzo, "Full duplex techniques for 5G networks: Self-interference cancellation, protocol design, and relay selection," *IEEE Commun. Mag.*, vol. 53, no. 5, pp. 128–137, May 2015.
[26] E. Everett, A. Sahai, and A. Sabharwal, "Passive self-interference suppression for full-duplex infrastructure nodes," *IEEE Trans. Wireless Commun.*, vol. 13, no. 2, pp. 680–694, Feb. 2014.
[27] M. Di Renzo, A. Zappone, M. Debbah, M.-S. Alouini, C. Yuen, J. de Rosny, and S. Tretyakov, "Smart radio environments empowered by reconfigurable intelligent surfaces: How it works, state of research, and the road ahead," *IEEE J. Sel. Areas Commun.*, vol. 38, no. 11, pp. 2450–2525, Nov. 2020.
[28] M. Jiang, Z. N. Chen, Y. Zhang, W. Hong, and X. Xuan, "Metamaterial-based thin planar lens antenna for spatial beamforming and multibeam massive MIMO," *IEEE Trans. Antennas Propag.*, vol. 65, no. 2, pp. 464–472, Feb. 2017.
[29] N. Shlezinger, G. C. Alexandropoulos, M. F. Imani, Y. C. Eldar, and D. R. Smith, "Dynamic metasurface antennas for 6G extreme massive MIMO communications," *IEEE Wireless Commun.*, vol. 28, no. 2, pp. 106–113, Apr. 2021.
[30] P. Mookiah and K. R. Dandekar, "Metamaterial-substrate antenna array for MIMO communication system," *IEEE Trans. Antennas Propag.*, vol. 57, no. 10, pp. 3283–3292, Oct. 2009.
[31] R. O. Ouedraogo, E. J. Rothwell, A. R. Diaz, K. Fuchi, and A. Temme, "Miniaturization of patch antennas using a metamaterial-inspired technique," *IEEE Trans. Antennas Propag.*, vol. 60, no. 5, pp. 2175–2182, May 2012.
[32] E. G. Korkontzila, D. B. Papafilippou, and D. P. Chrissoulidis, "Miniaturization of microstrip patch antenna for wireless applications by use of multilayered electromagnetic band gap substrate," in *Proc. 1st Eur. Conf. Antennas Propag.*, Nice, Nice, France, Nov. 2006, pp. 1–6.
[33] F. Chen, R. Morawski, and T. Le-Ngoc, "Self-interference channel characterization for wideband 2 × 2 MIMO full-duplex transceivers using dual-polarized antennas," *IEEE Trans. Antennas Propag.*, vol. 66, no. 4, pp. 1967–1976, Apr. 2018.
[34] J. H. Chen, L.-H. Ye, T. Liu and D.-L. Wu, "A low-profile dual-polarized patch antenna with simple feed and multiple decoupling techniques," *IEEE Antennas Wireless Propag. Lett.*, vol. 22, no. 8, pp. 1883–1887, Aug. 2023.
[35] J. Wu, M. Li, and N. Behdad, "A wideband, unidirectional circularly polarized antenna for full-duplex applications," *IEEE Trans. Antennas Propag.*, vol. 66, no. 3, pp. 1559–1563, Mar. 2018.
[36] D. Wu, Y.-X. Sun, B. Wang, and R. Lian, "A compact, monostatic, co-circularly polarized simultaneous transmit and receive (STAR) antenna with high isolation," *IEEE Antennas Wireless Propag. Lett.*, vol. 19, no. 7, pp. 1127–1131, Jul. 2020.
[37] D. Ahn, J.-S. Park, C.-S. Kim, J. Kim, Y. Qian, and T. Itoh, "A design of the low-pass filter using the novel microstrip defected ground structure," *IEEE Trans. Microw. Theory Techn.*, vol. 49, no. 1, pp. 86–93, Jan. 2001.
[38] A. Koc and T. Le-Ngoc, "Full-duplex mmWave massive MIMO systems: A joint hybrid precoding/combining and self-interference cancellation design," *IEEE Open J. Commun. Soc.*, vol. 2, pp. 754–774, 2021.
[39] S. Huberman and T. Le-Ngoc, "MIMO full-duplex precoding: A joint beamforming and self-interference cancellation structure," *IEEE Trans. Wireless Commun.*, vol. 14, no. 4, pp. 2205–2217, Apr. 2015.
[40] Y. Zhang, M. Xiao, S. Han, M. Skoglund, and W. Meng, "On precoding and energy efficiency of full-duplex millimeter-wave relays," *IEEE Trans. Wireless Commun.*, vol. 18, no. 3, pp. 1943–1956, Mar. 2019.
[41] Z. Luo, L. Zhao, L. Tonghui, H. Liu, and R. Zhang, "Robust hybrid precoding/combining designs for full-duplex millimeter wave relay systems," *IEEE Trans. Veh. Technol.*, vol. 70, no. 9, pp. 9577–9582, Sep. 2021.
[42] A. Koc and T. Le-Ngoc, "Intelligent non-orthogonal beamforming with large self-interference cancellation capability for full-duplex multiuser massive MIMO systems," *IEEE Access*, vol. 10, pp. 51771–51791, 2022.
[43] Y. Gong, R. Morawski, H. H. Lee, and T. Le-Ngoc, "A miniaturized 8 × 8 dual-layer EBG slotted circularly polarized patch antenna array for mMIMO," in *Proc. IEEE Global Commun. Conf.*, Dec. 2022, pp. 6511–6516.
[44] S. Ghosh, T.-N. Tran, and T. Le-Ngoc, "A dual-layer EBG-based miniaturized patch multi-antenna structure," in *Proc. IEEE Int. Symp. Antennas Propag. (APSURSI)*, Spokane, WA, USA, Jul. 2011, pp. 1828–1831.
[45] F. Yang and Y. Rahmat-Samii, "Microstrip antennas integrated with electromagnetic band-gap (EBG) structures: A low mutual coupling design for array applications," *IEEE Trans. Antennas Propag.*, vol. 51, no. 10, pp. 2936–2946, Oct. 2003.
[46] M. Mahmood, A. Koc, D. T. Nguyen, R. Morawski, and T. Le-Ngoc, "Sub-array selection in full-duplex massive MIMO for enhanced self-interference suppression," in *Proc. IEEE Global Commun. Conf. (GLOBECOM)*, Dec. 2023, pp. 1–6.

**YUANZHE GONG** (Graduate Student Member, IEEE) received the B.Eng. degree (Hons.) in electrical and computer engineering from McGill University, Montreal, QC, Canada, in 2020, where he is currently pursuing the Ph.D. degree in electrical engineering. Since 2018, he has been a Teaching Assistant with the Electrical and Computer Engineering Department, McGill University. His research interests include wireless communications, antenna design, metamaterial absorbers, massive MIMO, and full-duplex. He was a recipient of the McGill University Engineering Doctoral Award.

**MOBEEN MAHMOOD** (Graduate Student Member, IEEE) received the B.Sc. degree (Hons.) in electrical engineering from the University of Engineering and Technology (UET), Taxila, Pakistan, in 2013, and the M.Sc. degree (Hons.) electrical engineering from the American University of Sharjah (AUS), Sharjah, United Arab Emirates, in 2019. He is currently pursuing the Ph.D. degree in electrical engineering with McGill University, Montreal, QC, Canada. From 2014 to 2017, he was with China Mobile Pakistan (CMPak), Islamabad, Pakistan. His main research interests include massive MIMO, hybrid beamforming, UAV communications, AI-enable wireless networks, and full-duplex communications. He was a recipient of the AUS Teaching Assistantship, the AUS Research Assistantship, Fonds de Recherche du Qubec-Nature and Technologies (FRQNT), the IEEE VTS Student Travel Award, the IEEE Canada Vehicular Technologies Grant, the McGill Graduate Research Enhancement and Travel Award (GREAT Award), the McGill Graduate Excellence Fellowship, the McGill Engineering Class of 1936 Fellowship, and the J. W. McConnell Memorial Fellowship as part of McGill Engineering Doctoral Award (MEDA).

**ROBERT MORAWSKI** received the B.Sc. and M.Sc. degrees in electrical and computer engineering from Concordia University, Montreal, Canada, in 1997 and 2000, respectively. He is currently a Research Engineer and a Laboratory Manager with the Broadband Communications Research Laboratory, ECE Department, McGill University, Montreal. His research interest includes the design and implementation of prototype architectures for next-generation wireless communications.

**THO LE-NGOC** (Life Fellow, IEEE) received the B.Eng. degree in electrical engineering, in 1976, the M.Eng. degree in microprocessor applications from McGill University, Montreal, in 1978, and the Ph.D. degree in digital communications from the University of Ottawa, Canada, in 1983.

From 1977 to 1982, he was with SparAerospace Ltd., Sainte-Anne-de-Bellevue, QC, Canada, involved in the development and design of satellite communications systems. From 1982 to 1985, he was with SRTelecom Inc., Saint-Laurent, QC, where he developed the new point-to-multipoint DA-TDMA/TDM Subscriber Radio System SR500. From 1985 to 2000, he was a Professor with the Department of Electrical and Computer Engineering, Concordia University, Montreal. Since 2000, he has been with the Department of Electrical and Computer Engineering, McGill University. His research interest includes broadband digital communications.

Dr. Le-Ngoc is a Distinguished James McGill Professor; and a fellow of the Engineering Institute of Canada, the Canadian Academy of Engineering, and the Royal Society of Canada. He was a recipient of the 2004 Canadian Award in Telecommunications Research and the IEEE Canada Fessenden Award in 2005.